Structural analyses reveal that the ATG2A-WIPI4 complex functions as a membrane tether for autophagosome biogenesis

Saikat Chowdhury[1$], Chinatsu Otomo[1$], Alexander Leitner[2], Kazuto Ohashi[1#], Ruedi Aebersold[2,3,], Gabriel C. Lander[1]* and Takanori Otomo[1]*

[1]Department of Integrative Structural and Computational Biology, The Scripps Research Institute, La Jolla, CA 92037, USA

[2]Department of Biology, Institute of Molecular Systems Biology, Eidgenössische Technische Hochschule Zürich, 8093 Zurich, Switzerland

[3]Faculty of Science, University of Zurich, 8093 Zurich, Switzerland

*Correspondence authors: totomo@scripps.edu; glander@scripps.edu

$equal contribution

#Present address: Institute for Molecular and Cellular Regulation, Gunma University, Gunma, Japan

ABSTRACT

Autophagy is an enigmatic cellular process in which double-membrane autophagic compartments form *de novo* adjacent to the ER, sequestering cytoplasmic contents within and delivering them to lysosomes. Expansion of the precursor membrane phagophore requires autophagy-related 2 (ATG2), which localizes to the phosphatidylinositol-3-phosphate (PI3P)-enriched ER-phagophore junction. We combined single-particle electron microscopy, chemical cross-linking coupled with mass spectrometry, and biochemical analyses to characterize human ATG2A in complex with the PI3P effector WIPI4. ATG2A is a rod-shaped protein that can bridge neighboring vesicles through interactions at each tip of ATG2A. WIPI4 binds to one of the tips, enabling the ATG2A-WIPI4 complex to tether a PI3P-containing vesicle with another PI3P-free vesicle. These data suggest that ATG2A mediates ER-phagophore association and/or tethers vesicles to the ER-phagophore junction, prerequisites for phagophore expansion via the transfer of lipid membranes from the ER and/or the vesicles to the phagophore.

INTRODUCTION

Macroautophagy (hereafter autophagy) is a catabolic process essential for the maintenance of nutrition homeostasis and the elimination of cytotoxins, such as damaged organelles, invading bacteria, and aberrant protein aggregates [1, 2]. During autophagy, a double-membrane structure, termed the isolation membrane or phagophore, engulfs cytoplasmic contents or cargoes in a selective or non-selective manner [3]. The phagophore matures into the closed compartment autophagosome, resulting in sequestration of the cargoes from the cytoplasm. Subsequently, the autophagosome fuses with lysosomes, leading to the degradation of the cargoes and the recycling of the materials produced by the degradation, such as amino acids. Despite the critical importance of this cellular recycling system, a detailed understanding of the mechanisms of autophagosome biogenesis has been challenging to achieve due to the high complexity and unique nature of the underlying membrane reorganization steps.

A critical step is the expansion of the phagophore from a small punctum to a large cup-shaped structure, which presumably requires a continuous supply of lipid membranes as the phagophore expands. However, the origin of the lipid membranes has been controversial ever since autophagosomes were discovered [3]. On the one hand, vesicles from various cellular locations, such as plasma membrane, Golgi, endosome, and ER-Golgi intermediate compartment (ERGIC), have been shown to contribute to autophagosome formation [3-7]. However, whether these vesicles directly provide membranes for both the nucleation of the phagophore (punctum formation) and the subsequent expansion remains unclear. On the other hand, the ER and mitochondria have been suggested to provide membranes to the phagophore based on their observed association with the phagophore [4, 5, 8-18]. However, the association of the phagophore with mitochondria is only transient, whereas association with the ER is stable throughout phagophore biogenesis, implicating the ER as the provider of the bulk of the membranes.

Initiation of autophagy leads to the generation of the PI3P-enriched membrane named omegasome, which appears as an omega/ring-shaped subdomain of the ER under fluorescence images [16] or as a cluster of ER-associated thin tubular membranes under EM images [19]. The omegasome nucleates or recruits the first phagophore membrane and remains associated with the open end of the cup-shaped phagophore during its expansion [16]. When the phagophore has expanded sufficiently, the omegasome starts to shrink and finally disappears, which occurs concurrently with the sealing of the phagophore. The completed autophagosome promptly detaches from the ER and fuses with lysosomes. These observations suggest that the ER and the omegasome control phagophore biogenesis.

A role of the omegasome is to recruit ATG18, the PI3P effector that belongs to the PROPPIN (β-propellers that bind polyphosphoinositides) family [20, 21], and its binding protein ATG2 [22-24]. During phagophore expansion, both proteins are highly concentrated at the ER-phagophore junction [13, 14], while neither remains on the matured autophagosomes, indicating that they associate with the omegasome [22]. Depletion of mammalian ATG2A/B does not affect omegasome formation but causes an accumulation of small immature phagophores and small autophagosome-like vesicles distant from the ER [25]. This observation suggests that phagophore expansion requires ATG2 to be present concurrently with ER-phagophore association, implying that the ER is the provider of the bulk membranes.

A previous biochemical fractionation of yeast cells suggested that ATG2 may be a peripheral membrane protein [26]. Mammalian ATG2A/B also localize, in addition to the ER-phagophore junction, to lipid droplets (LDs) where they regulate the size of LDs [27, 28]. Such affinity of ATG2 with membranes suggests that ATG2 functions in mediating a membrane reorganization process, but its precise function is unknown. ATG2 is the largest ATG protein, spanning ~1600-2300 residues across eukaryotes. Little is known about the structure of ATG2 except that it contains three evolutionary conserved regions at the N- and C-terminus as well as in a middle region, all of which are registered in the Pfam database [29] as Chorein_N, ATG2_C, and ATG2_CAD, respectively (Fig. 1a). The first two regions share sequence similarities with VPS13 [27, 30], a paralog of which is VPS13A/Chorein [31]. ATG2_CAD contains a highly-conserved cysteine-alanine-aspartic acid triad. Notably, the functions of these domains are not known. A short (~100 residue) region preceding ATG2_C, which is also conserved but not registered in Pfam, is required for the localization of ATG2 to both phagophores and LDs [28]. We hereafter refer to this region as the C-terminal localization region or CLR.

To better understand the functional role of ATG2, we set out to characterize human ATG2A in complex with WIPI4, a mammalian paralog of ATG18, using structural and biochemical methods. A combination of electron microscopy (EM) and chemical cross-linking coupled with mass spectrometry (CXL-MS) experiments revealed that ATG2A has an elongated structure with the WIPI4 binding site at one end. We determined that ATG2A is a bipartite membrane-binding protein that bridges two membranes through interactions at each end (tips) of ATG2A. Furthermore, we demonstrate that the ATG2A-WIPI4 complex can mediate asymmetric tethering between liposomes with and without PI3P. Based on these findings, we propose that the ATG2-WIPI4 complex tethers the PI3P-enriched omegasome to a neighboring membrane, including the ER and the phagophore, as well as vesicles that may be recruited as a membrane source.

RESULTS

Reconstitution and overall structure of the human ATG2A-WIPI4 complex

To enable the structural characterization of ATG2 and investigate its interactions with ATG18/WIPIs, we generated human ATG2A and WIPI4, two proteins that have been reported to interact with each other tightly [28, 32, 33], from insect cells. The binding was confirmed by an affinity capture experiment in which WIPI4 was absorbed by beads loaded with ATG2A but not by beads lacking ATG2A (Fig. 1b), and a size exclusion chromatography measurement in which ATG2A and WIPI4 co-migrated (Fig. 1c). Negative-stain EM studies with the purified ATG2A-WIPI4 complex showed that the particles were monodisperse and homogenous in size and shape (Fig. S1). 2D class averages of the stained particles revealed that the ATG2A-WIPI4 complex is composed of a rod-shaped protein associated with a small, distinct bead-like feature at one end of the molecule (Fig. 1d). The structural details visible in the 2D averages suggest that the rod-shaped portion of the images corresponds to a multi-domain protein, and is likely ATG2A. The bead-shaped feature can be provisionally attributed to WIPI4 since the overall shape and size is consistent with its predicted β-propeller fold [34-36]. Comparison of these class averages with 2D averages of ATG2A alone supports this proposed organization (Fig. 1e) and establishes that ATG2A and WIPI4 form a stoichiometric complex upon reconstitution.

3D reconstructions of the ATG2A-WIPI4 complex and free ATG2A further support the 2D analyses, resolving a rod-shaped ATG2A about ~200 Å in length with a width of ~30Å. The rod has features like a “hook”-like shape and a cleft at its middle part (Fig. 1f, g). WIPI4 density was resolved with the characteristics of a negatively stained β-propeller and makes contact with ATG2A through a thin density (Fig. 1f). Such a contact likely serves as the pivot for WIPI4 to adopt a range of orientations relative to ATG2A, as observed in both 2D analyses (Movie S1) and 3D reconstructions (Fig. S1). Collectively, these results establish the overall structure of ATG2A in complex with WIPI4. WIPI4 is flexibly associated with ATG2A, inducing no significant conformational change to ATG2A.

The overall shape is conserved in yeast Atg2-Atg18 complex

The significance of the interactions between mammalian WIPIs and ATG2A/B has not been thoroughly studied. Much of our knowledge regarding this interaction comes from the studies on the *S. cerevisiae* ATG2-ATG18 complex. Thus, we investigated whether the structural organization of the human ATG2A-WIPI4 complex described above is conserved in the yeast complex. Yeast ATG2 is smaller than mammalian ATG2 (Fig. 1a) and appears to bind ATG18 weakly (Fig. S1), which makes the yeast complex more challenging for EM studies than its human counterpart. Nevertheless, we obtained 2D class averages of the ATG2-ATG18 complex (Fig. 1h), which show an elongated object with a bead-like density at one end, very similar to the human complex. These results confirm that the overall structure

of the ATG2-WIPI4/Atg18 complex is evolutionarily conserved from yeast to human, and indicate that functional studies in yeast are relevant in the context of structural work with the human version.

Identification of the WIPI4 binding site and insights into the chain topology of ATG2A

We used an integrative approach to gain further structural information on the ATG2A-WIPI4 complex. First, we sought to establish a coarse-grained chain trace of ATG2A and identify the sites of interaction between WIPI4 and ATG2A by CXL-MS. However, there were some foreseeable technical obstacles in performing a CXL-MS analysis of the ATG2-WIPI4 complex. For example, the overall 3D organization of the ATG2A-WIPI4 complex, comprising an elongated ATG2A and the small binding interface between ATG2A and WIPI4, limited the number of residue pairs that can be cross-linked. Furthermore, the protein complex was prone to aggregate at higher concentrations, limiting the highest protein concentration achievable without introducing aggregation to a moderate level for a CXL-MS analysis. Therefore, to maximize the number of the cross-linked pairs, we performed two cross-linking reactions: a standard amine-coupling reaction with disuccinimidyl suberate (DSS), which cross-links pairs of lysines up to ~30 Å apart [37], and another reaction with the coupling reagent 4-(4,6-dimethoxy-1,3,5-triazin-2-yl)-4-methylmorpholinium chloride (DMTMM) and a linker pimelic acid dihydrazide (PDH), which cross-links pairs of acidic and lysine residues with zero-length (ZL) or two acidic residues via PDH [38]. We used relatively low concentrations of the cross-linkers to suppress non-specific intermolecular cross-linking that would cause protein aggregation (see Methods). Despite these technical challenges, mass spectrometry of these samples successfully identified overall twenty cross-linked peptide fragments (Fig. 2a and Table S1). One each of DSS- and PDH-cross-links were identified within WIPI4, and both are consistent with the WIPI4 homology structure model (Fig. S2), validating our experiments. Fifteen cross-links were collected within ATG2A: eleven short to mid-range DSS/PDH/ZL-cross-links, which are indicative of locally-folded subdomains (Fig. 2a), as well as four long-range DSS cross-links between the residues in ATG_C and Lys720 or Lys1539. Because the DSS cross-linking did not result in dimerization or higher-order oligomerization of ATG2A (Fig. S3), we conclude that these long-range cross-links are intramolecular, suggesting that the folded ATG2A polypeptide adopts a non-linear chain topology. The last three cross-links were intermolecular between ATG2A and WIPI4: a DSS-cross-link between Lys1539 of ATG2A and Lys89 on Blade 2 of WIPI4 and two ZL cross-links between Asp1376 or Glu1378 of ATG2A and Lys134 on Blade 3 of WIPI4 (Fig. S2). These data agree with the previous work reporting that yeast ATG18 interacts with ATG2 through Blade 2 and Loop2 connecting Blades 2 and 3 [34, 39], suggesting an evolutionary conservation of this interaction mode. .

Second, we performed maltose binding protein (MBP) labeling of ATG2A. To map conserved regions on ATG2A, MBP was fused to ATG2A at either the N- or C-terminus, or inserted either between the CLR and the ATG_C (after the residue 1829) or within the ATG2_CAD (after residue 1224) (Fig. 2a). 2D image analyses revealed that the MBP of the first three constructs localized to the same tip of the complex, opposite the WIPI4-bound tip (Fig. 2b). The MBP inserted into the ATG2_CAD localized to the same tip as WIPI4 (Fig. 2b). Therefore, all three conserved regions are located at the tips of the elongated ATG2A structure. Hereafter, we refer to these tips as the NC tip and the CAD tip. We also inserted MBP into three positions adjacent to the residues cross-linked to WIPI4 (after residues 1344, 1373 and 1503) and found that all located in the proximity of WIPI4 (Fig. 2b), verifying the CXL-MS results.

Given that our EM structural analysis revealed that WIPI4 was flexibly attached to ATG2A, and the fact that β-propellers often bind to peptide, we next examined whether the WIPI4 binding site is in a flexible linear region of ATG2A. We generated a fragment of ATG2A (residues 1358-1404) containing two of the inter-molecularly cross-linked residues (Asp1375 and Glu1378) as a fusion to the B1 domain of streptococcal protein G (GB1) protein. The GB1-fused peptide co-migrated and eluted earlier than WIPI4 alone from a size exclusion chromatography column (Fig. 2c). The control with just GB1 and WIPI4 shows no co-migration, demonstrating that this peptide region is indeed capable of binding to WIPI4. Based on these results, we fit a WIPI4 homology model into the EM density, with Blade 2 facing ATG2A [34, 39] and the membrane-binding surface of WIPI4, including the two PI3P recognition sites (Blades 5 and 6) [34-36], on the opposite side of ATG2A (Fig. 2d).

ATG2A associates with membranes through its tips

Next, we sought to characterize membrane binding by ATG2A by performing a liposome flotation assay using a Nycodenz density gradient [40]. Small unilamellar vesicles (SUVs) or large unilamellar vesicles (LUVs) were mixed with ATG2A in the presence of Nycodenz, and centrifugation causes the liposomes to float to the top layer for collection and analysis. ATG2A rose to the top of the gradient only in the presence of liposomes (Fig. 3a), confirming direct membrane binding. The recovery of ATG2A proteins was substantially higher with SUVs than LUVs (14-32 fold with phosphatidylcholine (PC) vesicles), suggesting that ATG2A prefers binding to highly curved membranes. Additionally, incorporation of negatively charged lipid phosphatidylserine (PS) into the liposomes increased ATG2A-liposome association 1.3-9 fold, suggesting some electrostatic contribution to this interaction.

To better understand how ATG2A associates with membranes, we performed negative stain EM analysis on the ATG2A-WIPI4 complex bound to SUVs. Because ATG2A is a thin, somewhat featureless rod, we foresaw difficulties in clearly visualizing such proteins on large membrane surfaces.

Therefore, we added WIPI4 to serve as a molecular marker, allowing us to unambiguously determine the orientation of ATG2A bound to the liposomes. We used SUVs composed of only PC and PS, but not PI3P, to avoid any effects introduced by the WIPI4-PI3P interaction (note that WIPI4 does not bind to liposomes lacking PI3P [35]). In the raw micrographs (Fig. S4), we observed elongated objects resembling ATG2A associated with either one or two liposomes, as well as clustered liposomes. Focused 2D analyses on the elongated object well-resolved the features consistent with ATG2A bound to WIPI4, including the characteristic hook and cleft (Fig. 3b). The 2D classes could be categorized into three major structural classes of the protein-SUV complexes. In the first class, WIPI4 and the CAD tip of ATG2A are bound to the membrane, with the long axis of ATG2A aligned roughly orthogonally to the membrane, positioning the NC tip away from the membrane. In the second class, ATG2A is bound to the membrane through the NC tip, with the WIPI4 directed away from the membrane. These data indicate that both tips of ATG2A can interact with membranes independently of each other. Strikingly, particles belonging to the third class can be described as a combination of the first and second classes; ATG2A is bound to one liposome through the CAD tip and to another through the NC-tip, spacing neighboring liposomes ~10-15 nm apart. Thus, these EM data suggest that ATG2A is a bipartite membrane binding protein that can bridge two membranes.

ATG2A tethers SUVs

To test whether ATG2A is a *bona fide* membrane tether, we examined the effect of the presence of ATG2A on the size distribution of liposomes using dynamic light scattering (DLS). The DLS profile of the SUVs markedly shifted to larger sizes upon incubation with ATG2A (Fig. 4a), whereas those of the LUVs (100 and 400 nm) did not change (Fig. 4b, c). To confirm that the increase in the SUV particle size was due to liposome clustering mediated by the protein, we added proteinase K to the final sample of the ATG2-SUV mixture and monitored its effect. Upon incubation, the observed particle size decreased to its original starting point (Fig. 4d, e), demonstrating that homotypic tethering mediated by ATG2A resulted in the clustering.

We also performed a fluorescence-based liposome-tethering assay [41] in which biotin-incorporated liposomes were mixed with liposomes containing fluorescent lipids, and separated by streptavidin beads. The fluorescence intensity of the beads reports the degree of the tethering between these two kinds of liposomes. The results show that the fluorescence signals of the liposomes, regardless of size, were increased by the presence of ATG2A (Fig. 4f), but the difference between the signals in the presence or absence of ATG2A was ~5 times larger in the SUVs compared to the LUVs. These data suggest that ATG2A is capable of tethering liposomes, with a disposition for SUVs. In

combination, the results from flotation assays, DLS, and fluorescence measurements establish that ATG2A can tether small liposomes, i.e., membranes with a high curvature.

The CLR binds to membrane in an amphipathic helical conformation

The fact that the CLR in isolation localizes to LDs [28] raises the possibility that the CLR is a membrane-binding domain, as many proteins localize to LDs through a direct interaction with the lipid monolayer surface [42]. To further characterize the CLR with respect to lipid binding, we generated a CLR fragment as an MBP fusion construct to improve its solubility. In a liposome flotation assay, MBP-CLR was recoverable in the top fraction only in the presence of liposomes, whereas MBP alone was not, demonstrating direct membrane binding by the CLR (Fig. 5a). MBP-CLR associated with both SUVs and LUVs, indicating that the CLR is capable of binding to flatter membranes. Contrary to the strong preference of the full-length (FL) protein to SUVs (Fig. 3a), this result, though somewhat unexpected, is consistent with the LD localization of the CLR, as the diameters of LDs range from 100 nm to 100 mm [42]. We propose that the discrepancy is due to the difference in the affinity to LUVs. In vivo, FL ATG2A localizes to LDs, in addition to the phagophore-ER junction, in a CLR-mediated fashion [28], indicating that the FL protein can also bind to flatter membranes. However, biochemically isolated LDs do not contain ATG2A [28], suggesting a transient interaction between LDs and ATG2A, thus implying a weak affinity to flatter membranes. Notably, these data are in agreement with our observation that the FL protein weakly interacts with LUVs, particularly in the presence of PS (Fig. 3a). Possible explanations for the discrepancy are: 1) in the FL protein, the membrane-binding residues of the CLR may be partially occluded, 2) some of CLR fragment's hydrophobic residues, whose original roles are in the folding of the FL protein, may be exposed and available for membrane interaction as a consequence of the isolation as a fragment, or 3) the CLR's amphipathic helices in the FL may be held more rigidly than in the fragment, such that its curvature fit highly curved membranes well. Resolving this issue will require a high-resolution structure of the FL protein.

Because many LD-interacting proteins do so through an amphipathic helix [42], we sought to examine the secondary structure of the CLR. We purified a CLR-SUV complex by removing the MBP tag from the SUV bound MBP-CLR by proteolytic cleavage and performing a liposome flotation (Fig. 5b). The circular dichroism (CD) spectrum of the purified CLR-SUV complex shows a profile typical of an α-helix, with local minima at 208 and 220 nm (Fig. 5c). The helical wheel drawing of the CLR suggests that it can form an amphipathic α-helix (Fig. S5), supporting its affinity to membranes. The helical content predicted from the CD spectrum is 61%, and the CLR contains three proline residues in the middle of its sequence, suggesting that the CLR consists of several broken helices that are flexible. The conformation of the CLR, which is located within the polypeptide chain (rather than at a terminus),

could be more restricted in the FL protein, as the flanking regions of the CLR appear to be folded based on the CXL-MS results (Fig. 2a).

Together, these observations of the CLR and the FL constructs indicate that the CAD tip has a strong preference for highly curved membranes. The conserved region containing the CAD motif consists of ~200 residues with no similarity to any known domains or linear motifs, including the membrane curvature-sensing ALPS motif [43]. A deeper understanding of the mechanisms by which the CAD and the CLR interact with membranes will require high-resolution structural studies.

The ATG2A-WIPI4 complex tethers PI3P-containing and non-PI3P-containing membranes

The studies described above implicate a tethering function for ATG2A using membranes that lacked PI3P, the essential lipid concentrated at the ER-phagophore junction. Because the PI3P effector WIPI4 is located adjacent to only one of the two membrane-binding sites (the CAD tip), we hypothesized that the ATG2A-WIPI4 complex could bridge membranes with and without PI3P via WIPI4 and the CLR, respectively. Both WIPI4 [35] and the CLR fragment can interact with LUVs, while ATG2A alone cannot tether LUVs efficiently. Therefore, we sought to demonstrate PI3P-dependent tethering using LUVs. We first tested the homotypic tethering of PI3P-containing LUVs (100nm) using DLS. As shown in Fig. 6a and b, neither WIPI4 nor ATG2A individually changed the size distribution of the LUVs. Thus, the presence of PI3P does not appear to affect the affinity between the CAD tip and LUVs. In contrast, the LUV particle size increased markedly in the presence of both proteins (Fig. 6c, d), demonstrating that the WIPI4-PI3P interaction triggers the clustering of PI3P-containing LUVs.

To test the capacity for heterotypic tethering directly, we performed the fluorescence tethering assay with the LUVs containing PI3P and biotinylated lipids, and with LUVs lacking both. WIPI4 on its own did not change the fluorescence signal compared to the control (Fig. 6e). The addition of ATG2A showed only a slight increase in signal similar to what was observed using non-PI3P containing LUVs (Fig. 4f), demonstrating that the presence of PI3P does not improve ATG2A's poor ability to tether LUVs. In stark contrast, the signal increased markedly in the presence of the ATG2A-WIPI4 complex, with rises in fluorescence that were on par with what was observed for the homotypic tethering between non-PI3P-containing SUVs (Fig. 4f). Taken together, these data demonstrate heterotypic membrane tethering by the ATG2A-WIPI4 complex.

DISCUSSION

In the final stage of our manuscript preparation, Zheng et al. reported a related study on the rat ATG2B-WIPI4 complex [44], describing the overall shape of the ATG2B-WIPI4 complex by negative stain EM,

as well as PI3P-independent membrane binding by ATG2B. They also identified the WIPI4 binding site of ATG2A by a combination of CXL-MS and mutagenesis. Our findings are in agreement with the work from Zheng et al., and their mutational studies reinforce our identification of the WIPI4 binding site on ATG2A. However, we additionally demonstrate structurally and biochemically that ATG2A functions as a *bona fide* membrane tether, thereby illuminating a physical basis for autophagosome biogenesis. Combined with the localizations of ATG2 and ATG18/WIPIs to the ER-phagophore junction [13, 14] and their requirement for the ER-phagophore association [25], we propose that ATG2 together with ATG18/WIPI directly mediates the ER-phagophore association. While the precise localization of ATG2 within the ER-phagophore junction is not known, it would be logical to assume that ATG2 associates directly with the omegasome through its CAD tip as well as through WIPI/ATG18, as the omegasome consists of PI3P-enriched tubular membranes about ~30 nm in diameter [19], which is similar to the diameters of the SUVs used in this study (Fig. 7a). Although some PI3P molecules are also detected in the membranes of phagophores and even autophagosomes [45, 46], ATG18 and ATG2 are most strongly enriched at the ER-phagophore junction where the omegasome exists [13, 14]. Thus, it seems likely that the high abundance of PI3P and the high curvature of the omegasome membranes synergistically recruit the ATG2-ATG18/WIPI complex. Indeed, it has been reported that localizations of ATG2 and ATG18 in yeast are mutually dependent [22, 39], supporting this model. Our 2D averages of the ATG2A-WIPI4-SUV complex show that both the CAD and WIPI4 can simultaneously contact the same membrane (Fig. 3b), which also supports this model.

With the CAD tip attached to the omegasome, the CLR could bind to the ER exit site (ERES), which has been shown repeatedly in recent years as the exact location of the ER for the association with phagophore [13-15, 17, 18] (Fig. 7b). It was shown that the ERES undergoes dynamic membrane remodeling, possibly generating a membrane domain with a high-curvature. Alternatively, the CLR may be bound to the phagophore edge, which is likely to have a high membrane curvature. Although the CLR's membrane interactions are promiscuous, binding to membranes ranging in both composition and curvature, its affinity to membranes is higher with highly curved membranes. Thus, either of these membranes could be an ideal membrane substrate of the CLR. A previous cryo-EM tomographic study showed that the tubulovesicular omegasomes are connected to either the ER or the phagophore, and less frequently to both [19], which seems to be consistent with the dynamic association of the omegasome with the ER observed under fluorescence microscopy [16] and suggest that there exists a short-lived association between the omegasome with the phagophore. Thus, it may be probable that the CLR interacts alternately with the ERES and the phagophore edge, while the CAD tip remains bound to the omegasome, allowing the dynamic association of the omegasome with the ERES and the phagophore. Such shuttling of the omegasome between the ERES and the phagophore would imply

that the ER lipid membranes can be transferred to the omegasome upon the ERES-omegasome association and then to the phagophore upon the omegasome-phagophore association. Alternatively, the omegasome may mature into the new phagophore edge upon its association with the old edge. Both models are consistent with the observation in yeast that a significant amount of PI3P, which may originate from the omegasome, is delivered to the vacuole through autophagy [45]. Regardless of model, the transfer of ER lipid membranes to the phagophore would require VMP1, an ER membrane protein whose depletion impairs phagophore expansion similarly to ATG2 [25]. VMP1 appears to regulate ER membrane reorganizations at the contact sites with other organelles, such as mitochondria, endosomes, LDs and phagophores [24, 25, 47]. Thus, elucidation of the function of VMP1 and its potential interplay with ATG2 will shed light on the role of the ER in regulating organelle membranes including the phagophore.

Structurally, ATG2 shares no similarity with any canonical membrane tethers, such as dimeric coiled-coil proteins and multisubunit tethering complexes [48]. Furthermore, previously characterized canonical tethers are under control of the Rab family of small GTPases, while tethering by ATG2 would be regulated by PI3P through ATG18/WIPIs. These differences make ATG2 a unique membrane tether that is designed to coordinate the phagophore expansion and closure. As autophagosome formation nears completion, the omegasome collapses [16], which is presumably caused by the hydrolysis of PI3P, inducing the dissociation of the ATG2-ATG18/WIPI complex [22]. The phagophore closure and the detachment of the matured autophagosome from the ER occur concurrently with or immediately after the omegasome disaapprance [13, 16]. Such PI3P-regulated ER-phagophore tethering and its coupling with the expansion and closure steps provide a simple mechanism for the regulation of the size of autophagosomes by phosphatases, such as Ymr1 [49] and myotubularin [50]. How the release of ATG2 is mechanistically related to phagophore closure, a process that is facilitated by autophagic ubiquitin-like proteins [51], requires further investigation.

The membrane-tethering activity of ATG2 relies on the membrane-binding ability of the CAD and CLR, as well as the rod-shaped architecture. Notably, VPS13, which shares sequence similarity with ATG2 at the N- and C-terminus including the CLR, also possesses an elongated shape with dimensions similar to those of ATG2 as revealed by a recent negative-stain EM study [52]. The same study showed that VPS13 is required for the vesicular fusion in the trans-Golgi network (TGN) to endosome traffic as well as the homotypic fusion of TGNs [52]. VPS13 is also known to localize to organelle contact sites, including the ER-mitochondria contact site where VPS13 is thought to regulate membrane transfer from the ER to mitochondria [53-55]. Thus, both VPS13 and ATG2 function at membrane contact sites for mediating similar processes (lipid membrane transfer). Although VPS13 lacks the ATG2_CAD, it is tempting to speculate that VPS13 may also function as a membrane tether.

Apart from the proposed role of the ATG2-ATG18/WIPI complex in the ER-phagophore association, the complex may also play a role in recruiting other membrane source vesicles for phagophore expansion. ATG2 has been reported to interact with ATG9 and SEC23 (a component of COPII vesicle), the key components of the two kinds of vesicles required for nucleation of the phagophore and the omegasome [6, 7, 17, 56-58]. The integral membrane protein ATG9 is packaged into a small vesicle at Golgi, which arrives at the autophagosome-forming sites and associates with COPII vesicles. Notably, both ATG9 and COPII remain at the ER-phagophore junction, indicative of their participation in phagophore expansion. Because these vesicles are dynamic, it may be possible that ATG2 tethers these vesicles repeatedly to the omegasome through interactions with ATG9 and SEC23 to prime the SNARE-mediated membrane fusion [7, 59, 60]. The membranes incorporated into the omegasomes could be transferred to the connected phagophore for expansion as discussed above (Fig. 7b). This type of mechanism could operate simultaneously with membrane transfer from the ER.

Accession codes

The EM density maps of the ATG2A and ATG2A-WIPI4 complex are deposited to the EMDB with accession codes, 8900 and 8899, respectively.

Acknowledgements

We thank Drs. Imre Berger and Maria Martinez-Yamout for sharing the multibac system and cDNA of GB1, respectively, and Drs. Elizabeth M. Wilson-Kubalek and Zoltan Metlagel for assistance with preliminary experiments. This research was supported by the grants from the National Institute of Health (GM092740 to T.O. and DP2EB020402 to G.C.L.) and by the European Research Council (ERC) (AdvG grant 670821: Proteomics4D) to R.A. G.C.L. is supported as a Searle Scholar and a Pew Scholar.

Author contributions

S.C. collected and analyzed the EM data. C.O. expressed and purified proteins, and performed affinity capture experiments, liposome flotation assays, and fluorescence liposome tethering assays. A. L. collected and analyzed CXL-MS data. K.O. performed CD experiments. R. A. supervised the CXL-MS analysis. G.C.L. supervised the EM studies. T.O. conceived the overall project and performed EM sample preparation and DLS experiments. All authors contributed to the manuscript preparation.

Figures

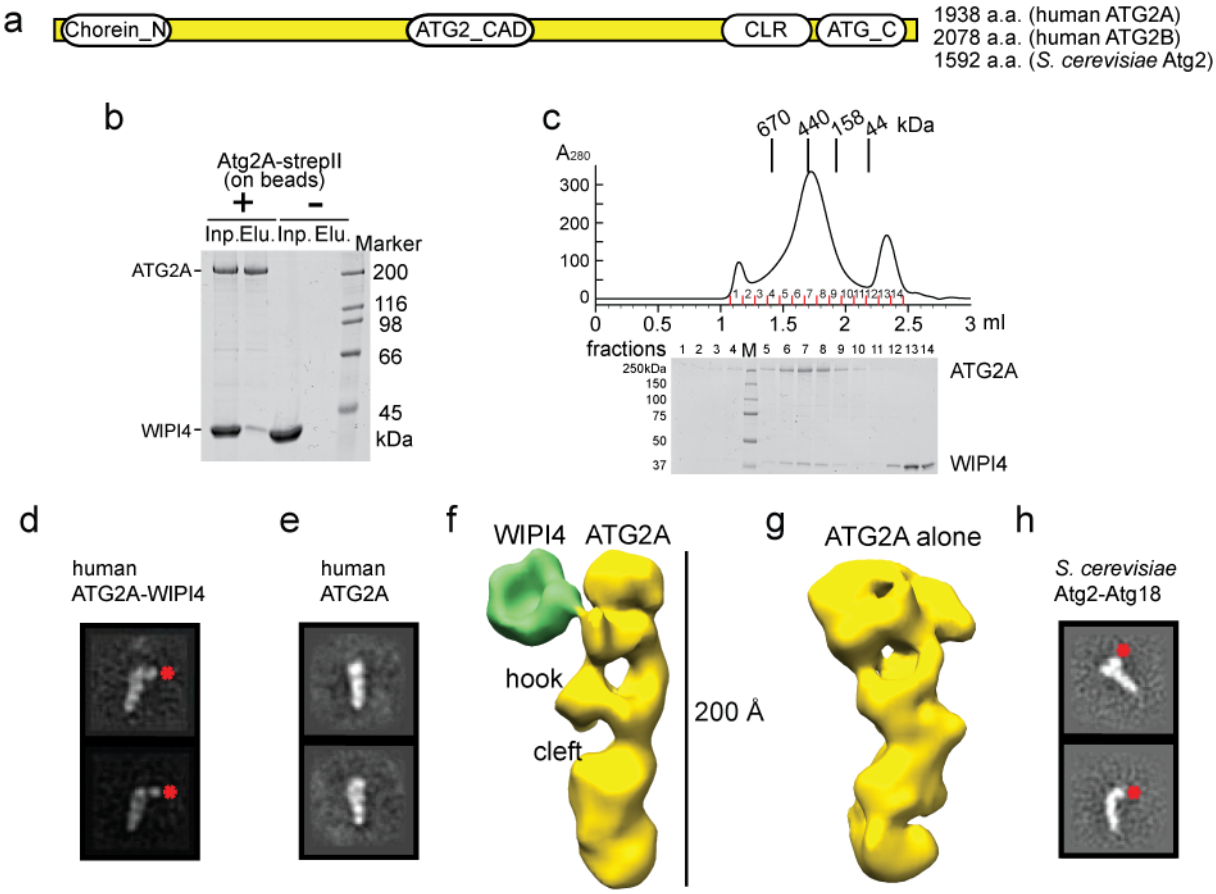

Fig. 1 Structural analyses of the human ATG2A-WIPI4 complex and *S. cerevisiae* ATG2-ATG18 complex by negative stain EM. (**a**) Diagram of the primary structure of ATG2. The lengths of human ATG2A/B and *S. cerevisiae* Atg2 are indicated. (**b**) Affinity capture experiment with ATG2A immobilized on the beads and WIPI4 in solution. (**c**) Superose 6 size exclusion chromatography profile of the mixture of ATG2A and an excess amount of WIPI4. (**d, e**) 2D class averages of the ATG2A-WIPI4 complex (**d**) and ATG2A alone (**e**). (**f, g**) Reconstructed 3D structures of the ATG2A-WIPI4 complex (**f**) and ATG2A alone (**g**). (**h**) 2D class averages of the *S. cerevisiae* ATG2-ATG18 complex. Red dots in 2D class averages indicate the locations of WIPI4 or ATG18, respectively.

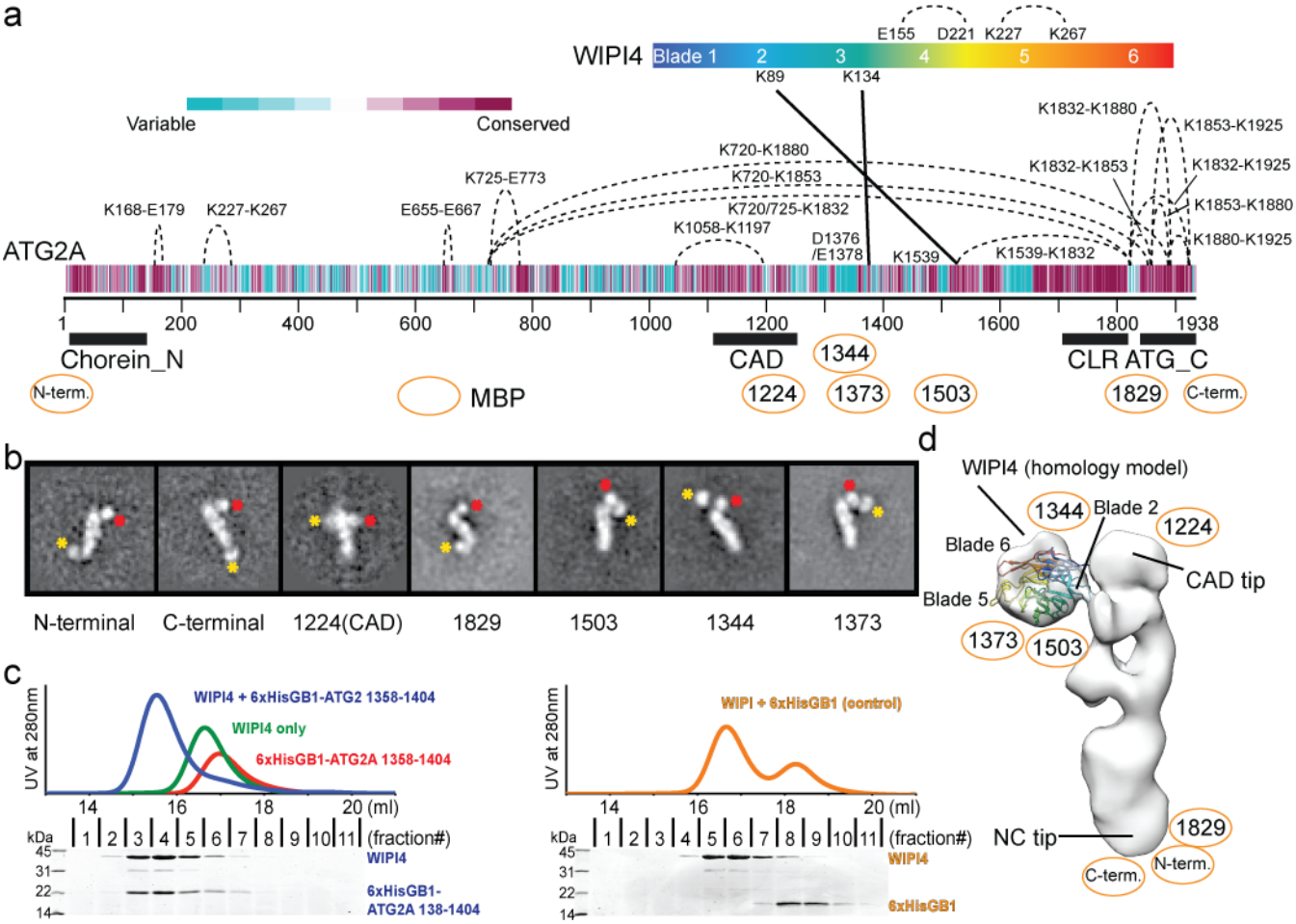

Fig. 2 Structural characterizations of the ATG2A-WIPI4 complex. (**a**) CXL-MS analysis of the ATG2A-WIPI4 complex. Intramolecular and intermolecular cross-links are indicated by dashed and solid lines, respectively. The cross-linked residues are labeled. The diagram of the primary structure of ATG2A is colored per the conservation score of each residue as indicated. The conservation score was calculated on ConSeq server[61]. Pfam conserved domains (Chorein_N, ATG2_CAD and ATG_C) and the CLR are indicated. (**b**) 2D class averages of MBP-fused or inserted ATG2A. All ATG2A constructs were visualized in the presence of WIPI4. The yellow asterisks and red dots indicate the locations of MBP and WIPI4, respectively. (**c**) Superdex 200 size exclusion chromatography profiles of 6xHis-GB1-ATG2A (1358-1404), WIPI4, 6xHis-GB1 and their mixtures as indicated. SDS-PAGE on left or right shows the fraction contents of the sample a mixture containing stoichiometric amounts of WIPI and 6xHis-GB1-ATG2A (1358-1404) or 6xHis-GB1 alone, respectively. (d) WIPI4-docked electron density map of the ATG2A-WIPI4 complex with labels of the MBP locations.

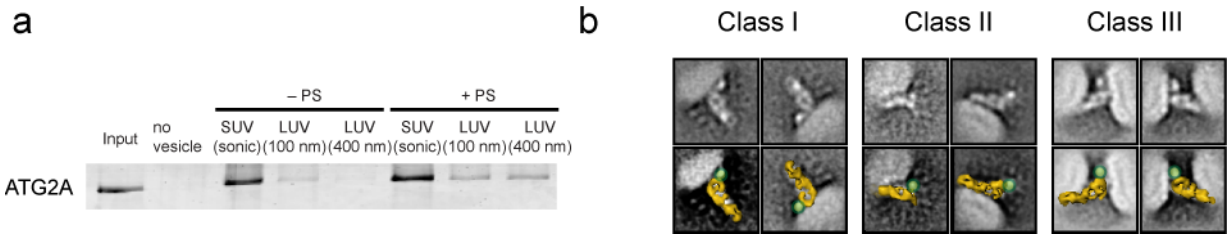

Fig. 3 Interaction between ATG2A and liposomes and its visualization by EM. (**a**) Liposome flotation assay with 50 nM ATG2A. The liposomes composed of 99% PC and 1% DiD (indicated as "–PS") or 74% PC, 25% PS and 1% DiD ("+PS") were prepared by sonication (SUVs) or extrusion (LUVs) using 100 or 400 nm filters. The inputs (4%) and the top layers after the centrifugation (24%) were loaded onto SDS-PAGE. The percentage of ATG2A recovered in each of the top fractions was quantified and is shown below the gel image. (**b**) 2D class averages of the ATG2A-WIPI4-SUV complex shown without (top) and with a manually placed 3D model of ATG2A (bottom, shown in yellow) together with a green dot on the WIPI4 density.

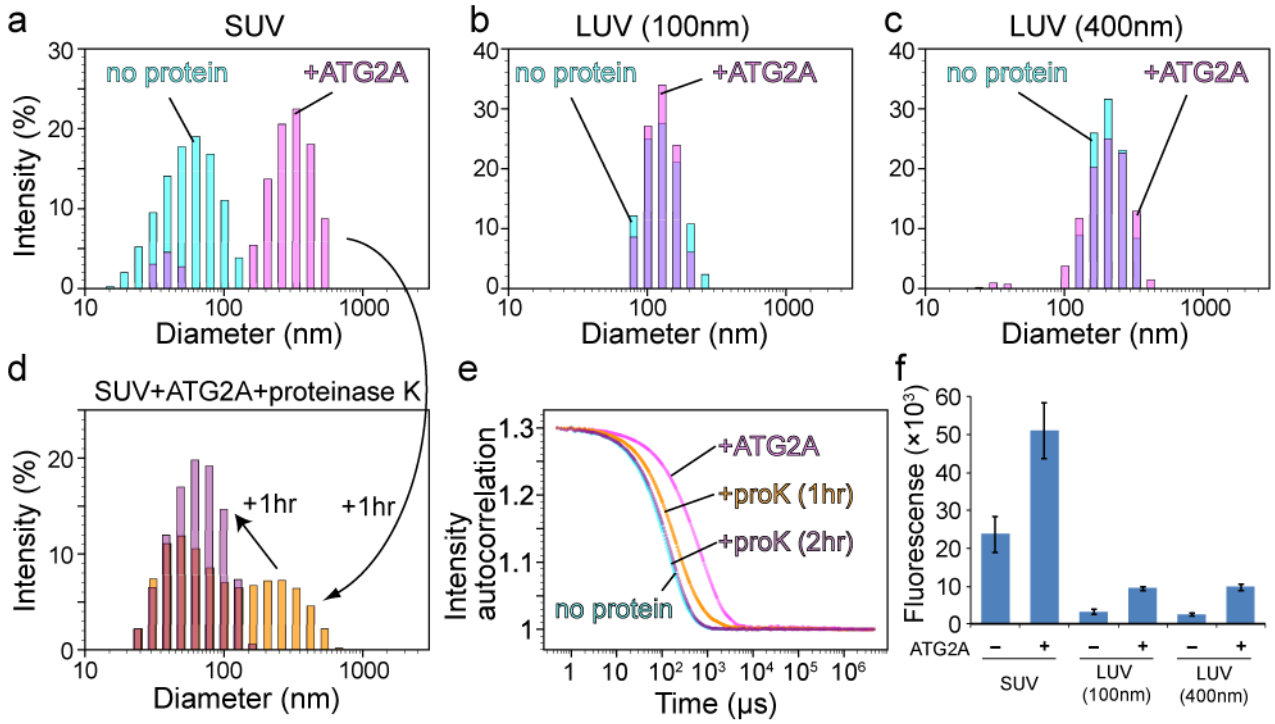

Fig. 4 Membrane tethering by ATG2A. (**a-c**) The DLS profiles of SUVs (**a**), LUVs (100 nm) (**b**), and LUVs (400 nm) (**c**) in the absence (cyan) or presence (magenta) of 200 nM ATG2A. All liposomes consisted of 75% PC and 25% PS. The samples were incubated for 1 hr before the measurements. (**d**) The final sample of (**a**) was mixed with proteinase K and re-measured upon 1 (yellow) and 2hr (purple) incubation. (**e**) Auto-scaled autocorrelation functions of the four DLS measurements with SUVs (**b, d**) are plotted. (**f**) Fluorescence liposome tethering assay. Liposomes consisting of 73.3% PC, 25% PS 0.2% biotinylated lipids, 1.5% Rhodamine-PE were mixed with liposomes with the same size consisting of 73% PC, 25% PS, 2% DiD in the presence of 200 nM ATG2A. The fluorescence reports the amount of the DiD-containing liposomes associated with the biotinylated liposomes. For each experiment, the average of three repeats is shown with the standard deviation.

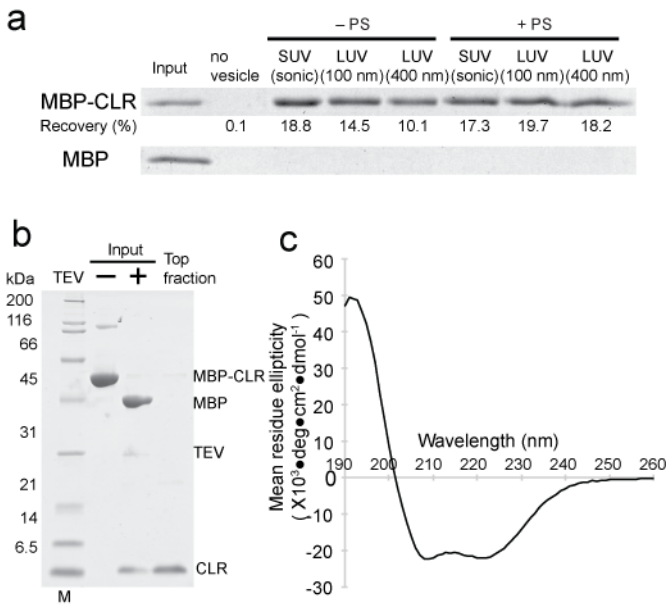

Fig. 5 Characterization of the CLR. (**a**) Liposome flotation assay with 100 nM MBP-fused ATG2A CLR (1723-1819) or MBP alone (control). The liposomes used are indicated as in Fig. 3a. The inputs (4%) and the top layers after the centrifugation (30%) were loaded onto SDS-PAGE. The percentage of MBP-CLR recovered in each of the top fractions was quantified and is shown below the gel image. (**b**) Preparation of the CLR-SUV complex by liposome flotation. The input containing MBP-CLR and SUVs (75% PC and 25% PS) was mixed with TEV to cleave off MBP, and the resulting CLR-SUV complex was isolated in the top fraction after centrifugation. (**c**) The CD spectrum of the CLR-SUV complex.

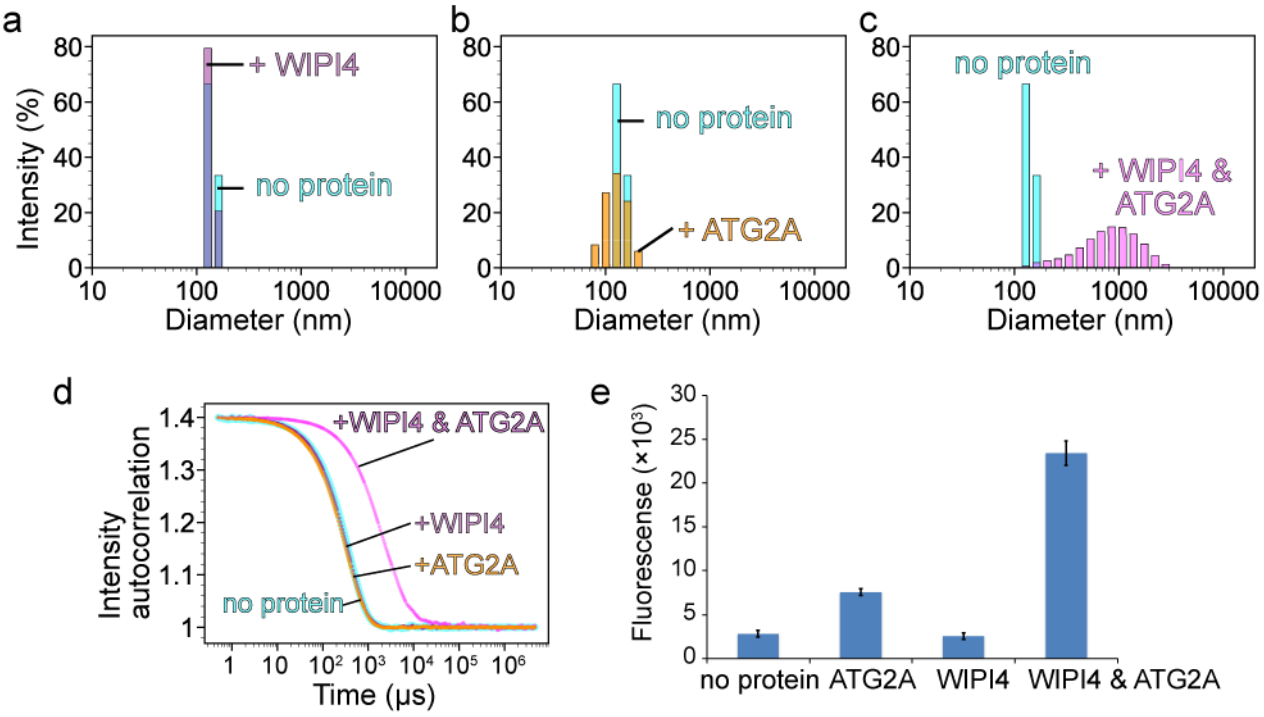

Fig. 6 Tethering of PI3P-containing LUVs by the ATG2-WIPI4 complex. (**a-c**) DLS profiles of LUVs (100 nm) consisting of 75% PC, 15% PS, 10% PI3P in the absence (**a-c**: cyan) or the presence of (**a**) 200 nM WIPI4, (**b**) 200 nM ATG2A, or (**c**) both proteins. (**d**) Auto-scaled autocorrelation functions of the four DLS measurements. (**e**) Fluorescence-based liposome tethering assay. Higher the fluorescence, more associations between the liposomes with and without PI3P. LUVs consisting of 73.3% PC, 15% PS, 10% PI3P, 0.2% biotinylated lipids, 1.5% Rhodamine-PE were mixed with LUVs consisting of 73% PC, 25% PS, 2% DiD in the presence of the indicated proteins. For each experiment, the average of three repeats is shown with the standard deviation.

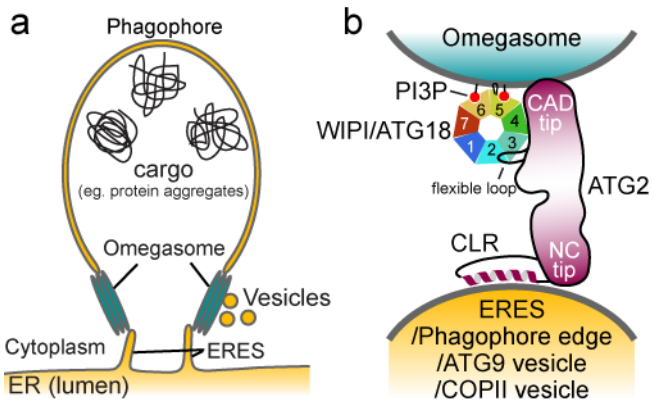

Fig. 7 Model of membrane tethering by the ATG2-WIPI/ATG18 complex at the ER-phagophore junction. (**a**) Illustration of the ER-phagophore junction based on current knowledge from cell biological studies. Each gray line represents a lipid bilayer. (**b**) Structural model of the ATG2-WIPI/ATG18 complex tethering the omegasome to its neighboring membranes (ERES, phagophore edge, ATG9 vesicle or COPII vesicle). The blackish red color of ATG2 represents conserved regions as similarly used in Fig. 2a. The WIPI/ATG18 binding region of ATG2 is represented as a black line emanating from the middle region of ATG2 to indicate the flexible attachment of WIPI/ATG18.

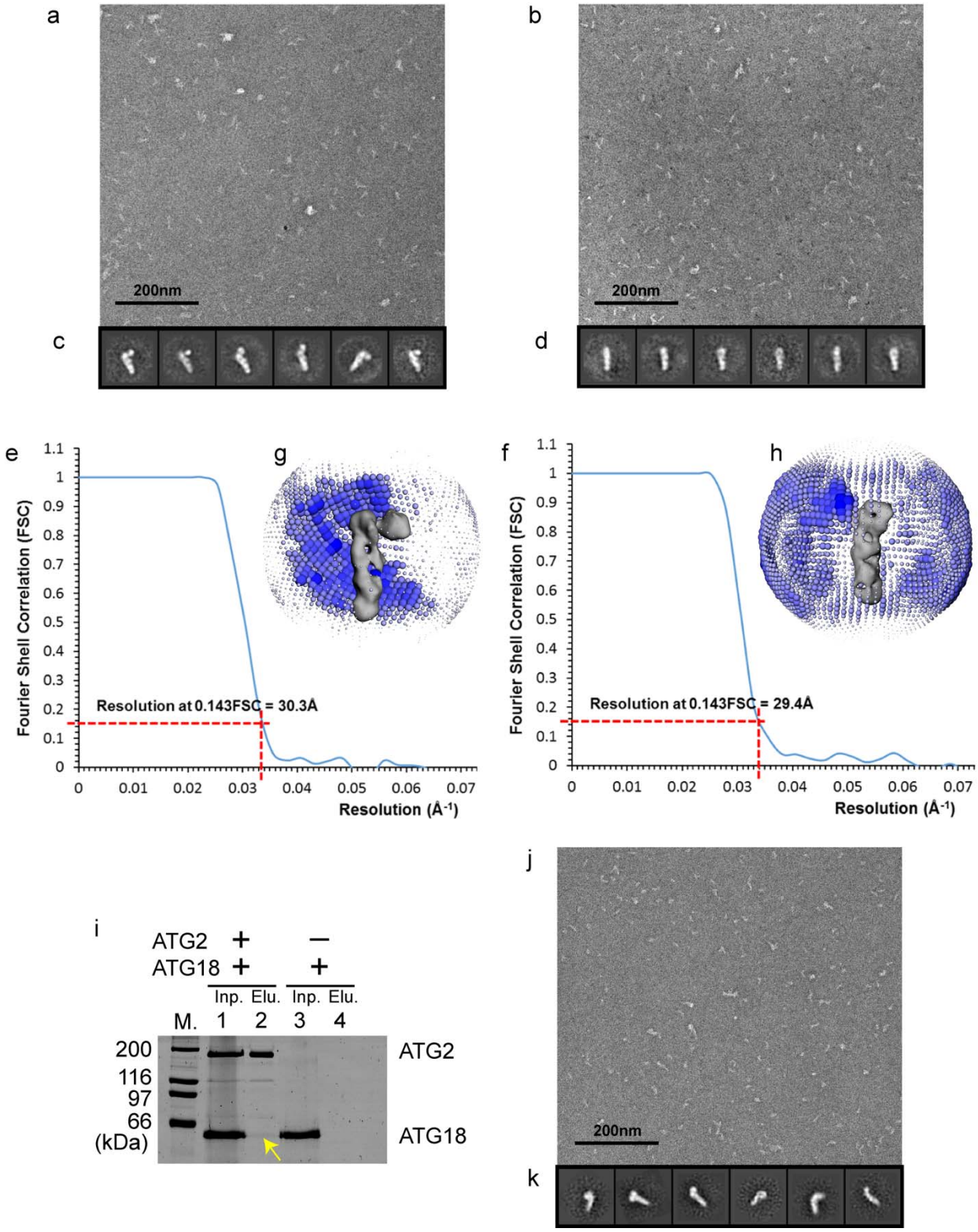
a
b
200nm
200nm
c
d
e
f
g
h
Fourier Shell Correlation (FSC)
Resolution (Å⁻¹)
Resolution at 0.143FSC = 30.3Å
Resolution at 0.143FSC = 29.4Å
i
ATG2 + −
ATG18 + +
Inp. Elu. Inp. Elu.
M. 1 2 3 4
200
116
97
66
(kDa)
ATG2
ATG18
j
k
200nm

Fig. S1 Negative-stain EM analyses of the human ATG2A-WIPI4 complex, free human ATG2A, and *S. cerevisiae* ATG2-ATG18 complex. (**a**, **b**) Representative electron micrographs of the ATG2A-WIPI4 complex (**a**) and free ATG2A (**b**) stained with 2% uranyl formate. (**c**, **d**) 2D class averages of the ATG2A-WIPI4 complex (**c**) and free ATG2A (**d**). (**e**, **f**) Fourier Shell Correlation (FSC) curves of the 3D reconstructions of the ATG2A-WIPI4 complex (**e**) and free ATG2A. (**g**, **h**) Euler angle distributions of the particles used for the final 3D reconstructions of the ATG2A-WIPI4 complex (**g**) and free ATG2A (**h**). (**i**) An affinity capture experiment with ATG2 immobilized on beads (Strep-Tactin) and ATG18 in solution. The experiment was performed as described in Methods for the same experiment with human proteins. Although the band of ATG18 in the elution from the beads loaded with ATG2 (lane2; indicated by an arrow) is faint, such band is completely absent in the control without ATG2 (lane 4), allowing us to conclude that the ATG18 band in the lane 2 is the proteins bound to ATG2. (**j**) A representative electron micrograph of the negatively stained elution sample of (**i**). (**k**) 2D class averages of the ATG2-ATG18 complex.

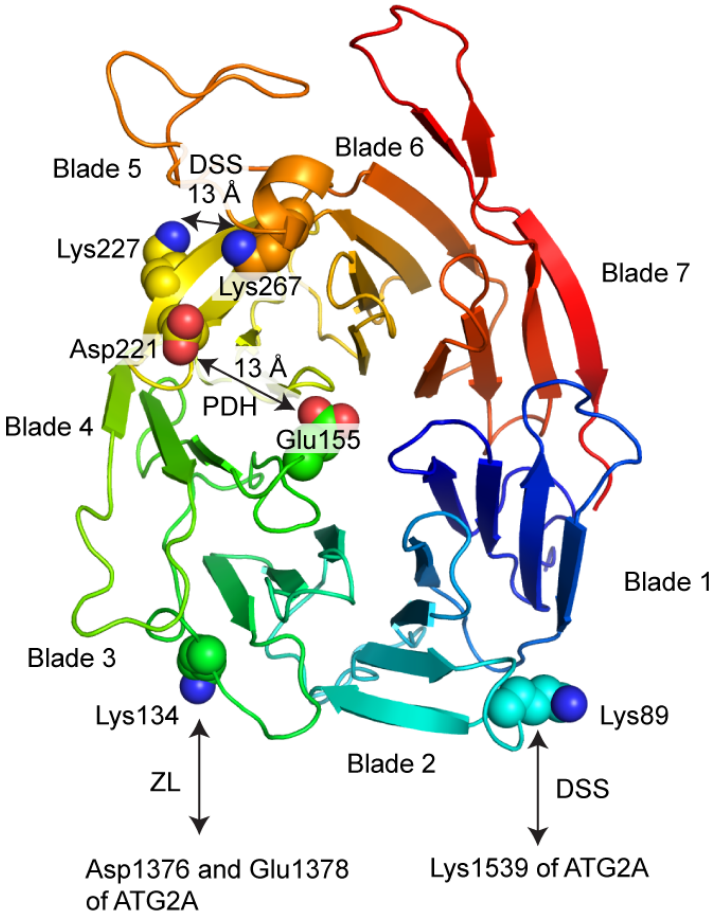

Fig. S2 Cross-linked positions of WIPI4. The residues cross-linked within WIPI4 or with ATG2A are shown with their side chains on the WIPI4 homology model. The two residues cross-linked by DSS (Lys227 and Lys267) or PDH (Glu155 and Asp221) are both ~13 Å apart, which is within reach of each cross-linker.

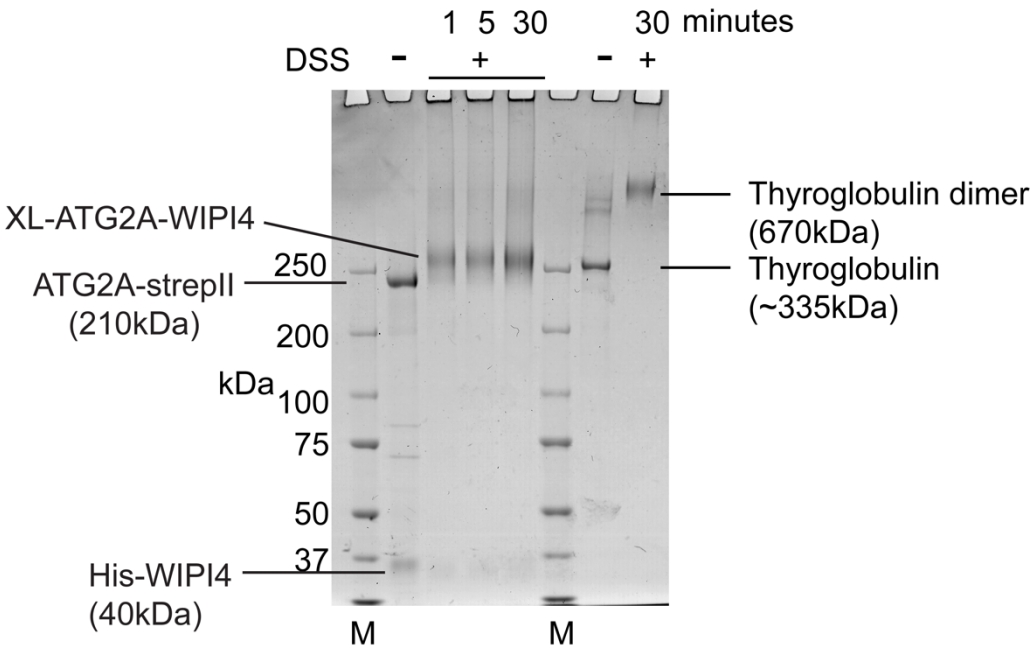

Fig. S3 SDS-PAGE analysis of DSS-cross-linking between ATG2A and WIPI4. A positive control reaction with ~350kDa thyroglobulin is shown in right.

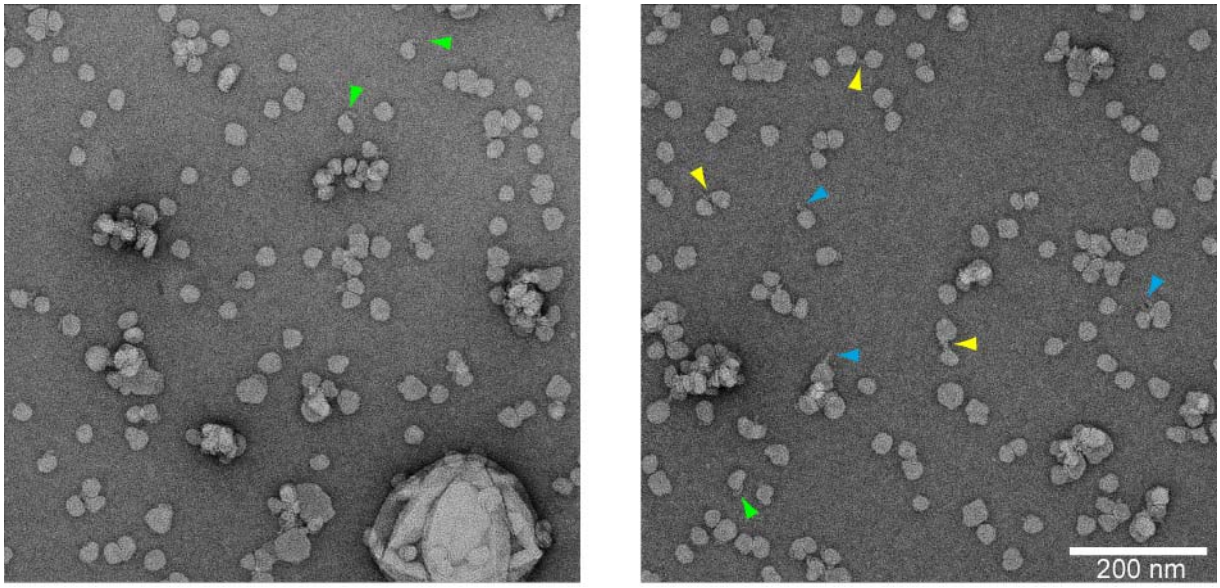

Fig. S4 Micrographs of the ATG2A-WIPI4-SUV complex. Blue, green and yellow arrowheads point at an elongated object that is emanating perpendicularly (blue) or tangentially (green) from an SUV, or is sandwiched by two SUVs (yellow).

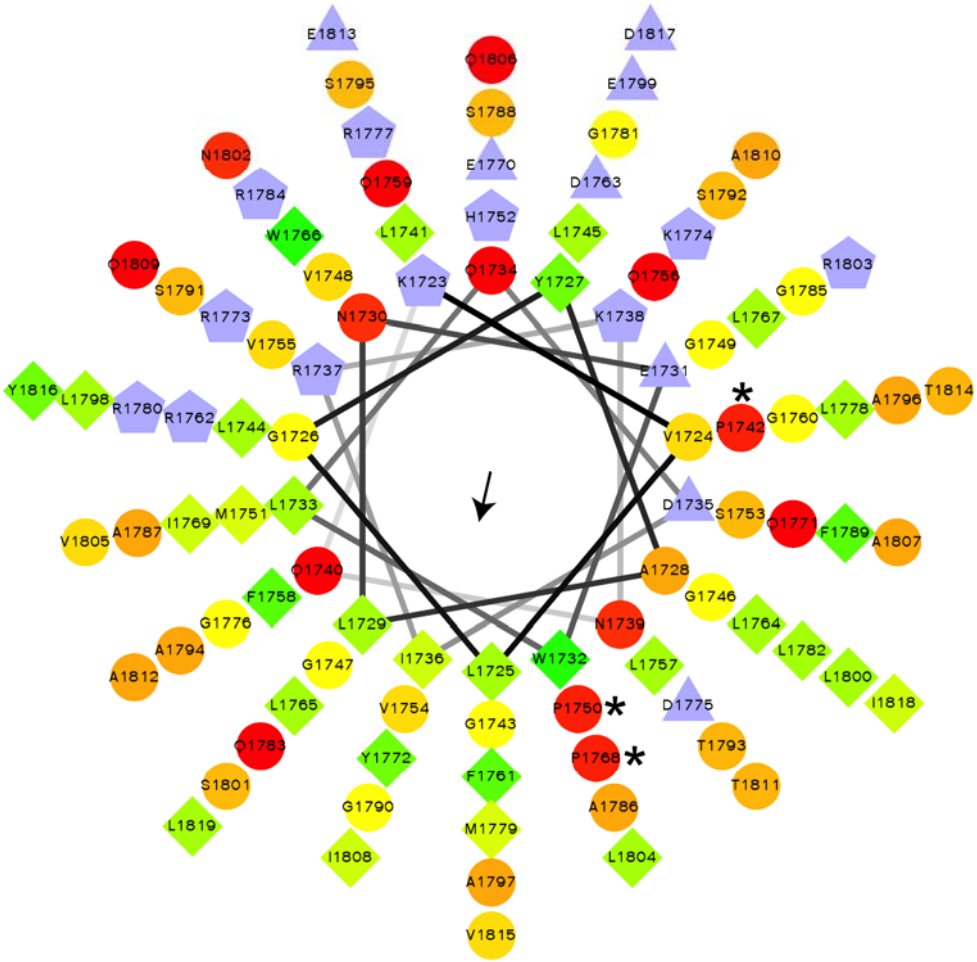

Fig. S5 The helical wheel drawing of the CLR (ATG2A 1723-1819). The hydrophobic moment [62] of the CLR is 0.299 and its direction is indicated by the arrow. The figure was generated using wheel.pl version 1.4 (http://rzlab.ucr.edu/scripts/wheel/wheel.cgi). Proline residues are indicated with an asterisk.

Table S1: List of cross-linked peptide fragments identified by CXL-MS

Linker	Id	Protein 1	Protein 2	AbsPos 1	AbsPos 2	Id-Score
DSS (Lys-Lys)	EGVAKAYDTVR-SLQDKR-a5-b5	ATG2A	ATG2A	1853	1832	33.87
	GTVHIFALKDTR-EKLVELR-a9-b2	WIPI4	WIPI4	267	227	33
	EGVAKAYDTVR-VSKALDPK-a5-b3	ATG2A	ATG2A	1853	720	29.83
	GHEQKGLTGAVGGVIR-SLQDKR-a5-b5	ATG2A	ATG2A	1880	1832	29.12
	GHEQKGLTGAVGGVIR-EGVAKAYDTVR-a5-b5	ATG2A	ATG2A	1880	1853	29.07
	VSKALDPK-SLQDKR-a3-b5	ATG2A	ATG2A	720	1832	28.63
	LASSQINKFLYLHTSER-SLQDKR-a8-b5	ATG2A	ATG2A	1539	1832	28.09
	NQIVPDAHKDHALK-EGVAKAYDTVR-a9-b5	ATG2A	ATG2A	1925	1853	28.02
	NQIVPDAHKDHALK-SLQDKR-a9-b5	ATG2A	ATG2A	1925	1832	27.64
	GHEQKGLTGAVGGVIR-NQIVPDAHKDHALK-a5-b9	ATG2A	ATG2A	1880	1925	26.65
	LASSQINKFLYLHTSER-EGKDSK-a8-b3	ATG2A	WIPI4	1539	89	26.32
	ALDPKSTGR-SLQDKR-a5-b5	ATG2A	ATG2A	725	1832	25.6
	GHEQKGLTGAVGGVIR-VSKALDPK-a5-b3	ATG2A	ATG2A	1880	720	20.96
PDH (Asp/Glu-Asp/Glu)	LRFPIADLRPER-AEQLR-a11-b2	ATG2A	ATG2A	655	667	30.11
	FPIADLRPER-AEQLR-a9-b2	ATG2A	ATG2A	655	667	27.31
	GLCDLCPSLEK-LFDTQSK-a10-b3	WIPI4	WIPI4	155	221	27.15
ZL (Lys-Asp/Glu)	DGEPVVTQLHPGPIVVR-KLFEFDTR-a3-b1	ATG2A	WIPI4	1378	134	30.45
	IKVTFLDTVVR-VEHSPGDGER-a2-b2	ATG2A	ATG2A	168	179	25.43
	EPEPSPFSSK-ALDPKSTGR-a3-b5	ATG2A	ATG2A	773	725	21.06
	DGEPVVTQLHPGPIVVR-KLFEFDTR-a1-b1	ATG2A	WIPI4	1376	134	20.94

Id; Assigned peptides and cross-linking sites within the *peptide* sequences. The longer peptide is designated as (a)lpha, the shorter as (b)eta. *Protein1*; The protein containing peptide designated as alpha. *Protein2*; The protein containing peptide designated as beta. *AbsPos1*; Position in the protein sequence of protein 1. *AbsPos2*; Position in the protein sequence of protein 2. *Id-score*; Identification score as assigned by xQuest.

Movie S1 WIPI4 (round lobe) is flexibly attached to ATG2A (rod-like density), as shown by aligning 2D averages of the complex to the density corresponding to ATG2A.

Materials and Methods

Protein expression and purification

Histidine-tagged human WIPI4 and *S. cerevisiae* ATG18 were expressed in *Spodoptera frugiperda* 9 (Sf9) cells using Bac-to-Bac system (Invitrogen). Cells were lyzed by a Dounce homogenizer or an Avestin C3 pressure homogenizer. After centrifugation at 40,000 × *g*, the proteins in the supernatant were purified by nickel affinity chromatography, followed by Source 15Q anion exchange chromatography and Superdex 200 size exclusion chromatography (GE Healthcare).

Human ATG2A and *S. cerevisiae* ATG2 were expressed with a GST tag and a StrepII tag at the N- and C-terminus, respectively, in Sf9 cells using multibac system [63], which was kindly provided by Dr. Imre Berger (EMBL). Cells were lysed and clarified as described above. The protein was loaded onto glutathione sepharose resin. After washing with a buffer containing 20 mM Tris-HCl pH 8.0, 500 mM NaCl, 0.5 mM TCEP, 20% Glycerol and 0.1% Triton-X100, the GST tag was cleaved off by TEV protease on the beads. The cleaved protein was eluted in the same buffer and loaded to StrepTactin affinity chromatography beads (IBA). The beads were washed extensively with 20 mM Tris-HCl pH 8.0, 150 mM NaCl, 0.5 mM TCEP to remove Triton X-100, followed by elution with the same buffer containing additional 5 mM desthiobiotin. The purified proteins were used for subsequent experiments immediately.

The C-terminal MBP fusion (ATG2A-MBP) and the ATG2A constructs into which an MBP was inserted were expressed with an N-terminal GST tag and purified similarly except that the last affinity step was replaced by Superose 6 size exclusion chromatography (GE Healthcare). The N-terminal MBP fusion of ATG2A (MBP-ATG2A) was fused with a histidine tag at the C-terminus and purified by nickel affinity chromatography, followed by Superose 6 size exclusion chromatography.

The CLR fragment (1723-1819) with an N-terminal His-MBP tag and a C-terminal intein-chitin binding domain tag was expressed in *E.coli* BL21(λDE3) from a modified pET vector (Novagen). Cells were lysed by an Avestin C3 homogenizer and clarified by centrifugation. The protein in the supernatant was absorbed onto chitin affinity beads (New England Biolabs). The intein tag was cleaved off on-beads with 40 mM DTT. His-MBP-CLR was eluted and further purified by Superdex 200 size exclusion chromatography and amylose affinity chromatography (New England Biolabs).

The WIPI4 binding fragment of ATG2A (1358-1404) was cloned into a pET vector modified for 6xHis-GB1 fusion. The fusion protein was expressed in *E.coli* BL21(λDE3) and purified by nickel affinity chromatography.

Affinity capture binding assay and reconstitution of the ATG2-WIPI4 complex for EM studies

StrepTactin Superflow beads loaded with ATG2A were mixed with His-WIPI4 in a buffer containing 20 mM HEPES pH 7.5, 150 mM NaCl, 0.5 mM TCEP, 20% glycerol, 0.1% Triton X-100. Beads were collected by centrifugation and washed with the same buffer three times. Proteins were eluted with the same buffer containing additional 5 mM desthiobiotin. The contents of the elution were examined by SDS-PAGE analysis (Fig. 1b). The control was carried out using the beads without ATG2A. For negative stain EM analyses, the beads loaded with ATG2A were washed and eluted in the same buffers excluding Trion X-100. For the MBP fusion/insertion constructs, the complexes were formed in solution by mixing ATG2A and a ~2-5-fold excess amount of WIPI4 and unbound WIPI4 was removed by size exclusion chromatography.

Reconstruction of the ATG2A-WIPI4-SUV complex

The lipid mixture (75% PC and 25% PS) was dried under nitrogen gas and vacuum dried. The obtained lipid film was dissolved in a buffer 20 mM Tris pH 8.0, 150 mM NaCl, 50 mM sodium cholate and dialyzed against the same buffer without sodium cholate. This dialysis procedure produced SUVs that were more homogenous than sonication method. The diameter of the SUVs was ~30 nm as determined by EM and DLS. To reconstitute the protein-SUV complex, ATG2A-StrepII was loaded onto StrepTactin beads. After a wash with 20 mM Tris pH 8.0, 150 mM NaCl, and 0.5 mM TCEP, WIPI4 was added to the beads. After 5 min incubation, the beads were washed again, and the liposomes were added, followed by another 10 min incubation. The beads were then washed with five column volumes, and the protein was eluted with 5 mM desthiobiotin. The eluted ATG2A-WIPI4-SUV complex was observed by negative stain EM as described below. Mixing the purified ATG2A-WIPI4 complex and the SUVs in solution also yielded a similar sample as determined by the negative stain EM while the data was collected using the sample reconstituted on beads (see below).

Negative Stain Electron Microscopy
Sample preparation

Continuous carbon grids for negative stain analyses were prepared by evaporating carbon onto nitrocellulose-coated 400 mesh Cu-Rh maxtaform grids (Electron Microscopy Sciences). For preparing each stained grid, a freshly glow-discharged grid was placed inversely on a 4 µL droplet of purified protein sample, which was sitting on a sheet of Parafilm, and incubated for 2 minutes. Most of the sample was wicked off with a filter paper (Whatman No. 1), and grids were immediately placed onto the surface of a 4 µL droplet of 2% (w/v) uranyl formate solution. After 5 seconds incubation, the grid was removed from the droplet, and excess stain was wicked off from the grid using filter paper. This staining step was repeated two more times. In the last staining step, the stain incubation time was extended to

30 seconds to thoroughly embed the protein sample in stain. Finally, after wicking off bulk stain the grid was completely air-dried on a piece of Parafilm. Grids for the protein-liposome complex were prepared similarly except that the initial incubation with the protein-liposome sample was extended to 5 minutes and 1% (w/v) uranyl acetate solution was used for staining.

Data acquisition

All the electron microscopy data were collected on a Tecnai Spirit (FEI) transmission electron microscope operating at 120keV, using a Tietz F416 CMOS, 4K × 4K camera (TVIPS). Data were acquired using the Leginon automated data acquisition system [64], using a nominal magnification of 52,000 ×, which yielded a pixel size of 2.05 Å at the detector level. Micrographs were collected using a total dose of ~30 electrons/Å^2, and with a defocus ranging from 1 µm to 1.5 µm. 1,407, 590, 441, 359, 626, 348, 440, 291, 409 and 1,805 micrographs were collected for ATG2A-WIPI4 complex, ATG2A alone, N-terminal-MBP tagged ATG2A-WIPI4 complex, C-terminal MBP-tagged ATG2A-WIPI4 complex, MBP tag at CADS (position 1224) of ATG2A-WIPI4 complex, MBP tag at position 1829 of ATG2A-WIPI4 complex, MBP tag at position 1503 of ATG2A-WIPI4 complex, MBP tag at position 1344 of ATG2A-WIPI4 complex, MBP tag at position 1373 of ATG2A-WIPI4 complex, and ATG2A-WIPI4 complex associated with liposome data sets respectively.

Image Processing

The Appion image-processing pipeline [65] was used to process the micrographs for all the datasets. CTFFind3 [66] was used for determining the contrast transfer function (CTF) of each micrograph. Particles were picked from the micrographs using Difference of Gaussians (DoG)-based automated particle picker [67], except the liposome-associated ATG2A-WIPI4 dataset, for which particles were manually picked from micrographs using the Manual Picker program in Appion. The phases of the micrographs were flipped using EMAN [68], and particles were extracted using a box size of 192 × 192 pixels for ATG2A, the ATG2A-WIPI4 complex, and yeast ATG2-ATG18 complex. A box size of 224 × 224 pixels was used for the extraction of all MBP-tagged ATG2A-WIPI4 complexes. For the liposome-bound ATG2A-WIPI4 complex dataset, a 160 × 160 pixel box, which incorporated the entire protein but only a fraction of liposome densities, was used. Particles for all the datasets were binned by a factor of two to speed up image processing. The extracted particle datasets were subjected to a topology-based reference-free 2D classification [69] in Appion, which was used to remove non-particle features and aggregates. The resulting stacks were used for subsequent analyses. To aid visualization of the flexible attachment of WIPI4 to ATG2A, we performed a masked classification that focused on the region surrounding the WIPI4 density using the Maskiton [70] web based classification server on a pre-aligned

stack of particles. The resulting 2D classes were used to create the movie depicting the flexible attachment of WIPI4 to ATG2 (Movie S1).

RELION1.4 [71] was used for 3D analyses of ATG2A and ATG2A-WIPI4 datasets, which contained 37,021 and 75,239 particles respectively. Particle stacks were normalized by eliminating pixels with values above or below 4.5σ of the mean pixel value using the normalization function in RELION, prior to 3D analysis. For 3D reconstruction of the ATG2A-WIPI4 dataset, a cylinder with similar dimensions (220Å in length and 50Å in diameter) as ATG2A was created using the "MO 3" function in the SPIDER [72] image processing program, which was used as an initial volume for a single-class initial 3D classification run in RELION. The resulting 3D class was used as an initial model for further 3D classification. Two rounds of 3D classification were performed to identify the best-resolved subset of particles. This subset was subsequently subjected to 3D auto-refinement by projection matching in RELION. For 3D processing of the ATG2A dataset, the final ATG2A-WIPI4 reconstruction was used as an initial model after 60Å low-pass filtering. This data set was initially subjected to three rounds of 3D classification and the best resolved subset of particles were then subjected to 3D auto refinement. Smoothed binary 3D masks were generated from the final refined volumes, extending the mask density by five pixels and applying an eight-pixel falloff. These masks were used to continue the 3D refinements to convergence. The final 3D reconstructions of ATG2A and the ATG2A-WIPI4 complex (Fig. 1f and g) had an estimated resolution of 29.4 Å and 30.3 Å (Fig. S1e and S1f) respectively, as assessed using Gold Standard Fourier Shell Correlation with a cutoff of 0.143. 6,386 and 5,317 particles contributed to the final reconstructions of ATG2A and the ATG2A-WIPI4 complex, respectively. 3D maps were visualized and segmented using UCSF Chimera [73]. The homology model of human WIPI4 was built from a crystal structure of *Kluyveromyces lactis* Hsv2p (Protein Data Bank code: 4EXV) using the software Modeller [74] and docked into the ATG2A-WIPI4 density using UCSF Chimera.

Focused 2D analysis of the liposome-bound ATG2A-WIPI4 complexes was performed using a similar methodology as described in earlier work [75], with the ISAC [76] 2D classification program. In this process, initial reference-free 2D classification of all the particles resulted in classes depicting the ATG2-WIPI4 complex either tethering two liposomes or attached to a single liposome. Particles belonging to these two types of classes were separated into two sub-stacks, each of which was subjected to reference-free 2D alignment using "sxali2d" program of the SPARX EM data processing package [77]. In this initial classification, the liposome electron microscopy density dominated the alignments. Based on the 2D averages of these aligned particles, binary masks were generated to eliminate density corresponding to the liposomes, enabling the 2D ISAC analyses to focus on the signal corresponding to the ATG2-WIPI4 complex. This resulted in class averages where the ATG2A-WIPI4

complexes were better resolved. The translational shifts and rotations determined in the masked analysis were then applied to the corresponding unmasked particles to generate unmasked 2D class averages containing well-resolved ATG2-WIPI4 complexes along with the associated liposomes (Fig. 3b (top row)). The ATG2-WIPI4 3D reconstructions were overlaid on these focused 2D class averages to annotate the different orientations of ATG2A (yellow density) -WIPI4 (green density) relative to the liposome (Fig. 3b (bottom row)).

Liposome flotation assay

Lipids (1,2-dioleoyl-*sn*-glycero-3-phosphocholine: PC and 1,2-dioleoyl-*sn*-glycero-3-phospho-L-serine: PS from Avanti Polar Lipids) and a dye, 1,1'-Dioctadecyl-3,3,3',3'-tetramethylindodicarbocyanine perchlorate (DiD) (Marker Gene Technologies), in chloroform were mixed at a molar ratio of PC:PS:DiD=99:0:1 or 74:25:1, and dried under nitrogen gas. DiD was included to enable visualization of the liposomes. The obtained lipid films were further dried under vacuum for 15-60 minutes, followed by hydration with a buffer containing 20 mM Tris pH 7.5, 150 mM NaCl. After hydration, the lipids were freeze-thawed seven times. For SUVs, the lipids were sonicated for ~90 seconds using a probe-type sonicator until the solution becomes translucent. For LUVs, the lipids were extruded through a polycarbonate filter with a pore size of 100 or 400 nm using an Avanti extruder. The flotation was carried out as reported previously [40]. In brief, a 300 µL mixture solution of 50 nM ATG2A, 300 µM liposomes and 40% (w/v) Nycodenz (Accurate Chemical) in 20 mM Tris pH 7.5, 150 mM NaCl, 0.5 mM TCEP was placed at the bottom of a centrifuge tube and a solution 250 µL of 30% Nycodenz in the same buffer was placed above the bottom solution. Finally, 50 µL of the same buffer without Nycodenz was placed on the top. The tubes were centrifuged in an SW55Ti rotor (Backman Coulter) at 279,982 × *g* (max) for 4 hours at 20˚C. After the centrifugation, the liposomes were visible in the top layer. The top fractions (75 µL) containing all the liposomes were collected and the contents were examined by SDS-PAGE. The gel was stained with Coomassie Brilliant Blue G-250 and scanned on a LI-COR Odyssey infrared imaging system. The bands were quantified using Image Studio 2.0 software.

CXL-MS analysis

The CXL-MS analysis was carried out as described previously [37, 38]. The ATG2A-WIPI4 complex was prepared at a concentration of 0.5 mg/ml in buffer containing 10 mM HEPES pH 7.5, 500 mM NaCl, 0.5 mM TCEP, 0.026 %(v/v) n-Dodecyl β-D-maltoside (DDM) and 20%(v/v) glycerol. For lysine-specific cross-linking, the pH was adjusted to 8.0 using 1 M HEPES pH 8.5. An equimolar mixture of DSS-d_0 and DSS-d_{12} (Creative Molecules Inc.) was added to the protein at a concentration of 0.25 mM and incubated at 37˚C for 30 min. For cross-linking of carboxyl groups and zero-length cross-linking, PDH-

d_0/d_{10} and DMTMM (both from Sigma-Aldrich) were added to final concentrations of 8.3 and 12 mg/mL, respectively, and the samples were also incubated at 37 °C for 30 min. The cross-linking reactions were stopped by diluting the samples four-fold with DDM-free buffer and removing the excess of cross-linking reagents with the help of Zeba gel filtration spin desalting columns (7K MWCO, Thermo Scientific). This step also helped to remove DDM, which could interfere with further processing steps and MS analysis. The filtrate was dried in a vacuum centrifuge. Samples were reduced, alkylated, and digestion with endoproteinase Lys-C and trypsin according to standard procedures, and purified digests were separated by peptide-level size-exclusion chromatography (Supexdex Peptide 3.2/30, GE). SEC fractions were analyzed by LC-MS/MS on an Easy nLC-1000 HPLC system and an Orbitrap Elite mass spectrometer (both from ThermoFisher Scientific). Data analysis was performed using xQuest [78] against a database containing the sequences of ATG2A, WIPI4 and contaminant proteins (tubulins, heat shock proteins and keratins).

DLS

DLS experiments were carried out with DynaPro Plate Reader II (Wyatt Technology). Solution mixtures containing 200 nM ATG2A and 60 µM (lipid) liposomes (75% PC and 25% PS, or 75% PC, 15% PS and 10% 1,2-dioleoyl-*sn*-glycero-3-phospho-(1'-myo-inositol-3'-phosphate) (PI3P)) in buffer 20 mM HEPES pH 7.5, 150 mM NaCl, 0.5 mM TCEP were incubated for an hour at 25˚C, followed by the DLS measurements with a laser power of 10%. In this condition, the protein alone did not produce measurable scattering, confirming that the DLS signals were from liposomes. Proteinase K (Sigma) was added to the clustered sonicated liposomes at a final concentration of 20 µg/ml, and the DLS was measured after 1 and 2 hours. All data were analyzed in the program DYNAMICS included in the instrument.

Fluorescence liposome tethering assay

Fluorescence liposome tethering assays were performed similarly as described previously [41]. For the experiments monitoring the tethering by ATG2A alone as shown in Fig. 4, two kinds of liposomes were prepared. One comprised 73.3% PC, 25% PS, 0.2% 1,2-distearoyl-*sn*-glycero-3-phosphoethanolamine-N-[biotinyl(polyethylene glycol)-2000] (DSPE-PEG(2000)-Biotin) and 1.5% 1,2-dioleoyl-*sn*-glycero-3-phosphoethanolamine-N-(lissamine rhodamine B sulfonyl) (Rhod-PE), and the other 73% PC, 25% PS and 2% DiD. SUVs and LUVs were prepared from each lipid mixture by sonication or extrusion. The former and the latter liposomes with the same size were mixed at a concentration of 60 µM (lipid) each in the presence or absence of 100 nM ATG2A. The mixture was incubated at room temperature for 5 min. Streptavidin MagneSphere resin (PROMEGA) was then added to the mixture. After 5 min

incubation, the resin was washed five times and resuspended in methanol. DiD fluorescence was normalized against rhodamine fluorescence to correct the difference of the total liposomes absorbed on the beads. For the experiments with PI3P and WIPI4 as shown in Fig. 6, LUVs with a lipid composition of 73.3% PC, 15% PS, 10% PI3P, 0.2% DSPE-PEG(2000)-Biotin and 1.5% Rhod-PE were mixed with those of 73% PC, 25% PS and 2% DiD.

CD spectroscopy

SUVs comprised of 75% PC and 25% PS were prepared by sonication and mixed with MBP-CLR at a molar ratio of protein:lipid=1:50. MBP was cleaved off by TEV protease, and the protein-SUV complex was purified by Nycodenz flotation as described above. The top fraction was dialyzed against the CD buffer consisting of 10 mM potassium phosphate pH 7.4, 150 mM potassium fluoride. After the dialysis, the sample was put into a cuvette with a path length of 1 mm. The final sample contained 6.7 μM CLR. The spectrum was acquired on an Aviv spectrophotometer at 25˚C. A sample containing only SUVs (335 μM lipid) was measured, and the resulting spectrum was used for background subtraction. The secondary structure contents were estimated by the program K2D3 [79].

References

1. Mizushima, N., T. Yoshimori, and Y. Ohsumi, *The role of Atg proteins in autophagosome formation.* Annu Rev Cell Dev Biol, 2011. **27**: p. 107-32.
2. Reggiori, F. and D.J. Klionsky, *Autophagic processes in yeast: mechanism, machinery and regulation.* Genetics, 2013. **194**(2): p. 341-61.
3. Lamb, C.A., T. Yoshimori, and S.A. Tooze, *The autophagosome: origins unknown, biogenesis complex.* Nat Rev Mol Cell Biol, 2013. **14**(12): p. 759-74.
4. Biazik, J., et al., *Ultrastructural relationship of the phagophore with surrounding organelles.* Autophagy, 2015. **11**(3): p. 439-51.
5. Hamasaki, M., et al., *Autophagosomes form at ER-mitochondria contact sites.* Nature, 2013. **495**(7441): p. 389-93.
6. Orsi, A., et al., *Dynamic and transient interactions of Atg9 with autophagosomes, but not membrane integration, are required for autophagy.* Mol Biol Cell, 2012. **23**(10): p. 1860-73.
7. Tan, D., et al., *The EM structure of the TRAPPIII complex leads to the identification of a requirement for COPII vesicles on the macroautophagy pathway.* Proc Natl Acad Sci U S A, 2013. **110**(48): p. 19432-7.
8. Hailey, D.W., et al., *Mitochondria supply membranes for autophagosome biogenesis during starvation.* Cell, 2010. **141**(4): p. 656-67.
9. Hayashi-Nishino, M., et al., *A subdomain of the endoplasmic reticulum forms a cradle for autophagosome formation.* Nat Cell Biol, 2009. **11**(12): p. 1433-7.
10. Dunn, W.A., Jr., *Studies on the mechanisms of autophagy: formation of the autophagic vacuole.* J Cell Biol, 1990. **110**(6): p. 1923-33.
11. Yla-Anttila, P., et al., *3D tomography reveals connections between the phagophore and endoplasmic reticulum.* Autophagy, 2009. **5**(8): p. 1180-5.
12. Zoppino, F.C., et al., *Autophagosome formation depends on the small GTPase Rab1 and functional ER exit sites.* Traffic, 2010. **11**(9): p. 1246-61.
13. Graef, M., et al., *ER exit sites are physical and functional core autophagosome biogenesis components.* Mol Biol Cell, 2013. **24**(18): p. 2918-31.
14. Suzuki, K., et al., *Fine mapping of autophagy-related proteins during autophagosome formation in Saccharomyces cerevisiae.* J Cell Sci, 2013. **126**(Pt 11): p. 2534-44.
15. Sanchez-Wandelmer, J., N.T. Ktistakis, and F. Reggiori, *ERES: sites for autophagosome biogenesis and maturation?* J Cell Sci, 2015. **128**(2): p. 185-92.
16. Axe, E.L., et al., *Autophagosome formation from membrane compartments enriched in phosphatidylinositol 3-phosphate and dynamically connected to the endoplasmic reticulum.* J Cell Biol, 2008. **182**(4): p. 685-701.
17. Karanasios, E., et al., *Autophagy initiation by ULK complex assembly on ER tubulovesicular regions marked by ATG9 vesicles.* Nat Commun, 2016. **7**: p. 12420.
18. Ge, L., et al., *Remodeling of ER-exit sites initiates a membrane supply pathway for autophagosome biogenesis.* EMBO Rep, 2017.
19. Uemura, T., et al., *A cluster of thin tubular structures mediates transformation of the endoplasmic reticulum to autophagic isolation membrane.* Mol Cell Biol, 2014. **34**(9): p. 1695-706.
20. Dove, S.K., et al., *Svp1p defines a family of phosphatidylinositol 3,5-bisphosphate effectors.* Embo J, 2004. **23**(9): p. 1922-33.
21. Proikas-Cezanne, T., et al., *WIPI proteins: essential PtdIns3P effectors at the nascent autophagosome.* J Cell Sci, 2015. **128**(2): p. 207-17.
22. Obara, K., et al., *The Atg18-Atg2 complex is recruited to autophagic membranes via phosphatidylinositol 3-phosphate and exerts an essential function.* Journal of Biological Chemistry, 2008.

23. Suzuki, K., et al., *Hierarchy of Atg proteins in pre-autophagosomal structure organization.* Genes Cells, 2007. **12**: p. 209-18.
24. Itakura, E. and N. Mizushima, *Characterization of autophagosome formation site by a hierarchical analysis of mammalian Atg proteins.* Autophagy, 2010. **6**(6): p. 764-776.
25. Kishi-Itakura, C., et al., *Ultrastructural analysis of autophagosome organization using mammalian autophagy-deficient cells.* Journal of cell science, 2014. **127**(Pt 18): p. 4089-4102.
26. Wang, C.W., et al., *Apg2 is a novel protein required for the cytoplasm to vacuole targeting, autophagy, and pexophagy pathways.* The Journal of biological chemistry, 2001. **276**(32): p. 30442-30451.
27. Pfisterer, S.G., et al., *Lipid droplet and early autophagosomal membrane targeting of Atg2A and Atg14L in human tumor cells.* J Lipid Res, 2014. **55**(7): p. 1267-1278.
28. Velikkakath, A.K., et al., *Mammalian Atg2 proteins are essential for autophagosome formation and important for regulation of size and distribution of lipid droplets.* Mol Biol Cell, 2012. **23**(5): p. 896-909.
29. Finn, R.D., et al., *The Pfam protein families database: towards a more sustainable future.* Nucleic Acids Res, 2016. **44**(D1): p. D279-85.
30. Yang, R.Y., et al., *Identification of VPS13C as a Galectin-12-Binding Protein That Regulates Galectin-12 Protein Stability and Adipogenesis.* PLoS One, 2016. **11**(4): p. e0153534.
31. Velayos-Baeza, A., et al., *Analysis of the human VPS13 gene family.* Genomics, 2004. **84**(3): p. 536-49.
32. Behrends, C., et al., *Network organization of the human autophagy system.* Nature, 2010. **466**(7302): p. 68-76.
33. Lu, Q., et al., *The WD40 repeat PtdIns(3)P-binding protein EPG-6 regulates progression of omegasomes to autophagosomes.* Dev Cell, 2011. **21**(2): p. 343-57.
34. Watanabe, Y., et al., *Structure-based analyses reveal distinct binding sites for Atg2 and phosphoinositides in Atg18.* J Biol Chem, 2012. **287**(38): p. 31681-90.
35. Baskaran, S., et al., *Two-site recognition of phosphatidylinositol 3-phosphate by PROPPINs in autophagy.* Mol Cell, 2012. **47**(3): p. 339-48.
36. Krick, R., et al., *PNAS Plus: Structural and functional characterization of the two phosphoinositide binding sites of PROPPINs, a -propeller protein family.* Proceedings of the National Academy of Sciences, 2012.
37. Leitner, A., T. Walzthoeni, and R. Aebersold, *Lysine-specific chemical cross-linking of protein complexes and identification of cross-linking sites using LC-MS/MS and the xQuest/xProphet software pipeline.* Nat Protoc, 2014. **9**(1): p. 120-37.
38. Leitner, A., et al., *Chemical cross-linking/mass spectrometry targeting acidic residues in proteins and protein complexes.* Proc Natl Acad Sci U S A, 2014. **111**(26): p. 9455-60.
39. Rieter, E., et al., *Atg18 function in autophagy is regulated by specific sites within its beta-propeller.* J Cell Sci, 2013. **126**(Pt 2): p. 593-604.
40. Nath, S., et al., *Lipidation of the LC3/GABARAP family of autophagy proteins relies on a membrane-curvature-sensing domain in Atg3.* Nat Cell Biol, 2014. **16**(5): p. 415-24.
41. Ragusa, M.J., R.E. Stanley, and J.H. Hurley, *Architecture of the Atg17 complex as a scaffold for autophagosome biogenesis.* Cell, 2012. **151**(7): p. 1501-12.
42. Thiam, A.R., R.V. Farese, Jr., and T.C. Walther, *The biophysics and cell biology of lipid droplets.* Nat Rev Mol Cell Biol, 2013. **14**(12): p. 775-86.
43. Drin, G., et al., *A general amphipathic alpha-helical motif for sensing membrane curvature.* Nat Struct Mol Biol, 2007. **14**(2): p. 138-46.
44. Zheng, J.X., et al., *Architecture of the ATG2B-WDR45 complex and an aromatic Y/HF motif crucial for complex formation.* Autophagy, 2017: p. 0.
45. Obara, K., et al., *Transport of phosphatidylinositol 3-phosphate into the vacuole via autophagic membranes in Saccharomyces cerevisiae.* Genes Cells, 2008. **13**(6): p. 537-47.

46. Cheng, J., et al., *Yeast and mammalian autophagosomes exhibit distinct phosphatidylinositol 3-phosphate asymmetries.* Nat Commun, 2014. **5**: p. 3207.
47. Tabara, L.C. and R. Escalante, *VMP1 Establishes ER-Microdomains that Regulate Membrane Contact Sites and Autophagy.* PLoS One, 2016. **11**(11): p. e0166499.
48. Baker, R.W. and F.M. Hughson, *Chaperoning SNARE assembly and disassembly.* Nat Rev Mol Cell Biol, 2016. **17**(8): p. 465-79.
49. Cebollero, E., et al., *Phosphatidylinositol-3-phosphate clearance plays a key role in autophagosome completion.* Curr Biol, 2012. **22**(17): p. 1545-53.
50. Taguchi-Atarashi, N., et al., *Modulation of local PtdIns3P levels by the PI phosphatase MTMR3 regulates constitutive autophagy.* Traffic, 2010. **11**(4): p. 468-78.
51. Tsuboyama, K., et al., *The ATG conjugation systems are important for degradation of the inner autophagosomal membrane.* Science, 2016. **354**(6315): p. 1036-1041.
52. De, M., et al., *The Vps13p-Cdc31p complex is directly required for TGN late endosome transport and TGN homotypic fusion.* J Cell Biol, 2017. **216**(2): p. 425-439.
53. Lang, A.B., et al., *ER-mitochondrial junctions can be bypassed by dominant mutations in the endosomal protein Vps13.* J Cell Biol, 2015. **210**(6): p. 883-90.
54. Park, J.S., et al., *Yeast Vps13 promotes mitochondrial function and is localized at membrane contact sites.* Mol Biol Cell, 2016. **27**(15): p. 2435-49.
55. Murley, A. and J. Nunnari, *The Emerging Network of Mitochondria-Organelle Contacts.* Mol Cell, 2016. **61**(5): p. 648-53.
56. Ge, L., et al., *The ER-Golgi intermediate compartment is a key membrane source for the LC3 lipidation step of autophagosome biogenesis.* Elife, 2013. **2**: p. e00947.
57. Ge, L., M. Zhang, and R. Schekman, *Phosphatidylinositol 3-kinase and COPII generate LC3 lipidation vesicles from the ER-Golgi intermediate compartment.* Elife, 2014. **3**: p. e04135.
58. Yamamoto, H., et al., *Atg9 vesicles are an important membrane source during early steps of autophagosome formation.* J Cell Biol, 2012. **198**(2): p. 219-33.
59. Lemus, L., et al., *An ER-Localized SNARE Protein Is Exported in Specific COPII Vesicles for Autophagosome Biogenesis.* Cell Rep, 2016. **14**(7): p. 1710-22.
60. Nair, U., et al., *SNARE proteins are required for macroautophagy.* Cell, 2011. **146**(2): p. 290-302.
61. Berezin, C., et al., *ConSeq: the identification of functionally and structurally important residues in protein sequences.* Bioinformatics, 2004. **20**(8): p. 1322-4.
62. Eisenberg, D., R.M. Weiss, and T.C. Terwilliger, *The helical hydrophobic moment: a measure of the amphiphilicity of a helix.* Nature, 1982. **299**(5881): p. 371-4.
63. Bieniossek, C., et al., *MultiBac: expanding the research toolbox for multiprotein complexes.* Trends Biochem Sci, 2012. **37**(2): p. 49-57.
64. Suloway, C., et al., *Automated molecular microscopy: the new Leginon system.* J Struct Biol, 2005. **151**(1): p. 41-60.
65. Lander, G.C., et al., *Appion: an integrated, database-driven pipeline to facilitate EM image processing.* J Struct Biol, 2009. **166**(1): p. 95-102.
66. Mindell, J.A. and N. Grigorieff, *Accurate determination of local defocus and specimen tilt in electron microscopy.* J Struct Biol, 2003. **142**(3): p. 334-47.
67. Voss, N.R., et al., *DoG Picker and TiltPicker: software tools to facilitate particle selection in single particle electron microscopy.* J Struct Biol, 2009. **166**(2): p. 205-13.
68. Ludtke, S.J., P.R. Baldwin, and W. Chiu, *EMAN: semiautomated software for high-resolution single-particle reconstructions.* J Struct Biol, 1999. **128**(1): p. 82-97.
69. Ogura, T., K. Iwasaki, and C. Sato, *Topology representing network enables highly accurate classification of protein images taken by cryo electron-microscope without masking.* J Struct Biol, 2003. **143**(3): p. 185-200.
70. Yoshioka, C., et al., *Maskiton: Interactive, web-based classification of single-particle electron microscopy images.* J Struct Biol, 2013. **182**(2): p. 155-63.

71. Scheres, S.H., *RELION: implementation of a Bayesian approach to cryo-EM structure determination.* J Struct Biol, 2012. **180**(3): p. 519-30.
72. Shaikh, T.R., et al., *SPIDER image processing for single-particle reconstruction of biological macromolecules from electron micrographs.* Nat Protoc, 2008. **3**(12): p. 1941-74.
73. Goddard, T.D., C.C. Huang, and T.E. Ferrin, *Visualizing density maps with UCSF Chimera.* J Struct Biol, 2007. **157**(1): p. 281-7.
74. Webb, B. and A. Sali, *Comparative Protein Structure Modeling Using MODELLER.* Curr Protoc Bioinformatics, 2014. **47**: p. 5 6 1-32.
75. Chowdhury, S., et al., *Structural organization of the dynein-dynactin complex bound to microtubules.* Nat Struct Mol Biol, 2015. **22**(4): p. 345-7.
76. Yang, Z., et al., *Iterative stable alignment and clustering of 2D transmission electron microscope images.* Structure, 2012. **20**(2): p. 237-47.
77. Hohn, M., et al., *SPARX, a new environment for Cryo-EM image processing.* J Struct Biol, 2007. **157**(1): p. 47-55.
78. Walzthoeni, T., et al., *False discovery rate estimation for cross-linked peptides identified by mass spectrometry.* Nat Methods, 2012. **9**(9): p. 901-3.
79. Louis-Jeune, C., M.A. Andrade-Navarro, and C. Perez-Iratxeta, *Prediction of protein secondary structure from circular dichroism using theoretically derived spectra.* Proteins, 2012. **80**(2): p. 374-81.